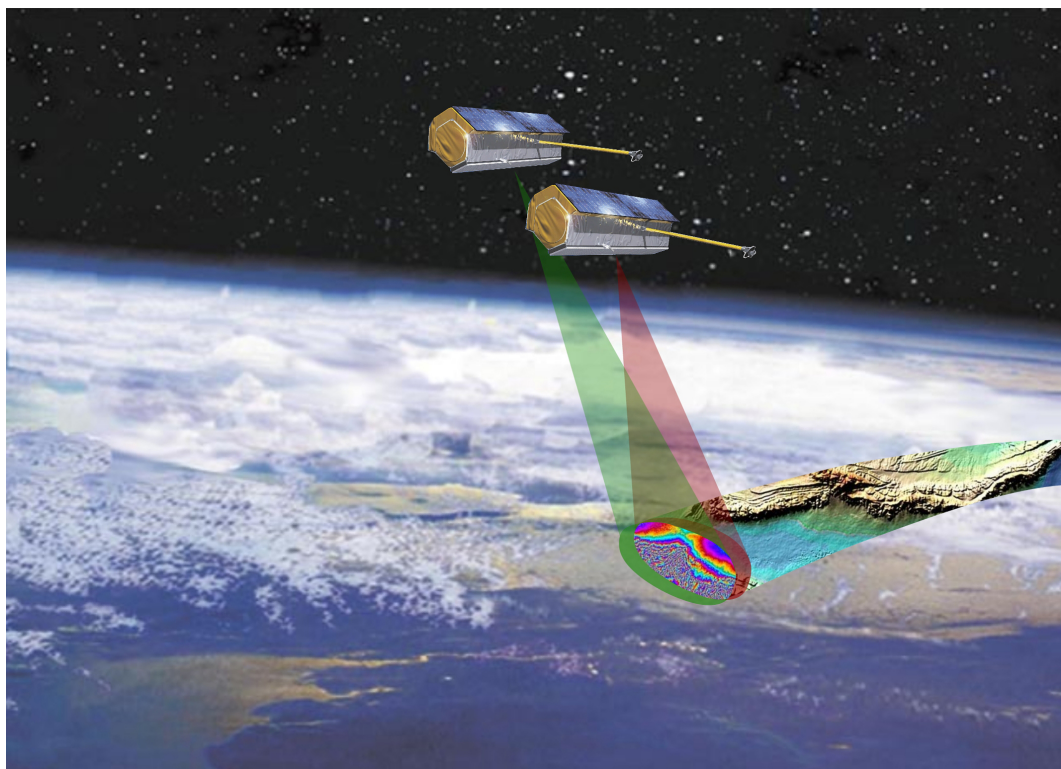


# Satellite Formation Flying for High-Precision Earth Observation

Pol Francesch Huc, Sydney Hsu



AA 279D - Spacecraft Formation-Flying and Rendezvous  
Stanford University

## Revision History

Table 1: Summary of project revisions.

Rev	Changes
PS1	<ul style="list-style-type: none"><li>- Created document</li><li>- Added problem set 1 material</li></ul>
PS2	<ul style="list-style-type: none"><li>- Added problem set 2 material</li><li>- Revised PS1 orbital elements and updated document accordingly</li></ul>
PS3	<ul style="list-style-type: none"><li>- Added problem set 3 material</li></ul>

## Contents

<b>0 Scope</b>	<b>7</b>
<b>1 Problem Set 1</b>	<b>7</b>
1.1 Problem 1: Your Mission, Your Challenge . . . . .	7
1.1.a Reference Mission . . . . .	7
1.1.b Mission Objectives . . . . .	7
1.1.c Spacecraft Specification . . . . .	8
1.1.d Launch and Orbit . . . . .	8
1.1.e Synthetic Aperture Radar Payload . . . . .	9
1.1.f Key Dynamics, Guidance, Navigation & Control Requirements . . . . .	10
1.2 Problem 2: Orbit Simulation, Review of Astrodynamics . . . . .	10
1.2.a Initial Orbital Elements . . . . .	10
1.2.b Initial Position and Velocity . . . . .	11
1.2.c Unperturbed and J2 Propagation Numerical Simulations . . . . .	12
1.2.d Unperturbed Numerical and Analytical Comparison . . . . .	12
1.2.e Osculating Orbital Elements from Numerical Simulation . . . . .	14
1.2.f Mean Classical Orbital Elements . . . . .	16
1.2.g Reconciling Osculating and Mean Orbital Elements . . . . .	18
<b>2 Problem Set 2</b>	<b>19</b>
2.1 Problem 1: Everything is Relative . . . . .	19
2.1.a Chief and Deputy Orbit Initialization . . . . .	19
2.1.b Numerical Integration of Relative Equations of Motion . . . . .	19
2.1.c Analytical Solution to Fundamental Orbital Differential Equations . . . . .	22
2.1.d Numerical and Analytical Comparison . . . . .	23
2.1.e Drift Correction Maneuver . . . . .	26
2.1.f Maneuver Simulation . . . . .	26
<b>3 Problem Set 3</b>	<b>28</b>
3.1 Problem 1: We are Close in Near-Circular Orbits . . . . .	28
3.1.a Initial Conditions . . . . .	28

3.1.b	Initial Position and Velocity . . . . .	28
3.1.c	Hill-Clohessy-Wilshire Integration Constants . . . . .	28
3.1.d	HCW in Rectilinear Coordinates . . . . .	29
3.1.e	HCW in Rectilinear Coordinates . . . . .	30
3.2	Problem 2: We are Close in Eccentric Orbits . . . . .	31
3.2.a	Initial Conditions . . . . .	31
3.2.b	Yamanaka-Ankersen Integration Constants . . . . .	31
3.2.c	Yamanaka-Ankersen Solution . . . . .	32
3.2.d	Discussion of YA Solution . . . . .	34
3.2.e	Quasi-Nonsingular Relative Orbit Elements . . . . .	34
3.2.f	Relative Orbital Elements Geometric Linear Mapping . . . . .	34
3.2.g	Comparison between Relative Orbital Elements and YA Integration Constants . .	37
3.2.h	True Relative Propagation . . . . .	37
3.2.i	Difference in Semi-major Axis & Highly Eccentric Orbits . . . . .	39
<b>4</b>	<b>References</b>	<b>43</b>
<b>5</b>	<b>Appendix A: Code</b>	<b>44</b>

## List of Figures

1	TerraSAR-X spacecraft features. [3]	8
2	Helix satellite formation of TerraSAR-X and TanDEM-X illustrating relative orbits (left) and cross-track baselines as a function of orbit position (right). [2]	9
3	Data acquisition modes: Monostatic (left), bistatic (middle), and alternating bistatic (right). [2]	10
4	Simulated TDS orbital path starting on 15 June 2007 (1000 orbits).	12
5	Absolute position and velocity errors of the numerical integration with respect to the analytical solution in the RTN frame.	14
6	Orbital elements, specific angular momentum, and specific energy over 5 orbits for J2 (blue) and unperturbed (red) propagation.	15
7	Line of apsides and specific angular momentum over 5 orbits for J2 (blue) and unperturbed (red) propagation.	16
8	Orbital elements, specific angular momentum, and specific energy over 5 orbits for J2 (blue), unperturbed (red), and mean classical (yellow) orbit propagation.	17
9	Line of apsides and specific angular momentum over 5 orbits for J2 (blue), unperturbed (red), and mean classical (yellow) orbit propagation.	17
10	Isolating seemingly unperturbed parameters of the mean classical orbit propagation reveals small precession.	18
11	Numerically integrated relative RTN position of the deputy (TDX) with respect to the chief (TSX) using the non-linear equations of relative motion.	20
12	Numerically integrated relative RTN velocity using the non-linear equations of relative motion.	21
13	Overlaid numerically integrated (blue) and analytically determined (red) relative RTN position.	22
14	Overlaid numerically integrated (blue) and analytically determined (red) relative RTN velocity.	23
15	Position error in the RTN frame between the numerical and analytical solutions.	24
16	Velocity error in the RTN frame between the numerical and analytical solutions.	24
17	Position error between the numerical and analytical solutions with a difference in initial semi-major axis.	25
18	Numerically integrated relative RTN position with a difference in initial semi-major axis.	25
19	Numerically integrated relative RTN position before (blue) and after (red) the maneuver.	27
20	Numerically integrated relative RTN velocity before (blue) and after (red) the maneuver.	27
21	Numerically integrated relative RTN position from HCW equations over 15 orbits.	29

---

22	Numerically integrated relative RTN velocity from HCW equations over 15 orbits. . . . .	30
23	Along-track drift apparent in HCW solution over 50 orbits. . . . .	30
24	Analytically solved relative RTN position from YA solution over 15 orbits. . . . .	33
25	Analytically solved relative RTN velocity from YA solution over 15 orbits. . . . .	33
26	Analytically solved relative RTN position from YA solution. . . . .	34
27	Analytically solved relative RTN position from YA solution (blue) and geometric linear mapping (red). . . . .	36
28	Analytically solved relative RTN velocity from YA solution (blue) and geometric linear mapping (red). . . . .	36
29	Analytically solved relative RTN position from YA solution (blue), geometric linear mapping (red), and numerical integration (yellow). . . . .	38
30	Analytically solved relative RTN velocity from YA solution (blue), geometric linear mapping (red), and numerical integration (yellow). . . . .	38
31	Error in the analytically solved relative RTN velocity from YA solution (blue), and geometric linear mapping (red). . . . .	39
32	Analytically solved relative RTN position from YA solution (blue), geometric linear mapping (red), and numerical integration (yellow) for non-energy matched chief and deputy. .	40
33	Analytically solved relative RTN position from YA solution (blue), geometric linear mapping (red), and numerical integration (yellow) for large initial relative separation. . . . .	41
34	Analytically solved relative RTN position from YA solution (blue), geometric linear mapping (red), and numerical integration (yellow) for non-energy matched chief and deputy. .	42

## List of Tables

1	Summary of project revisions. . . . .	1
2	Comparison of DTED-2 and HRTE-3 specifications [2] . . . . .	7
3	Initial orbital parameters of TSX and TDX in Helix formation. . . . .	19
4	Differences in initial orbit elements. . . . .	28

## 0 Scope

This report introduces the project, mission specifications, and orbit simulations for AA279D Dynamics, Navigation and Control of Distributed Space Systems.

## 1 Problem Set 1

### 1.1 Problem 1: Your Mission, Your Challenge

#### 1.1.a Reference Mission

This project is based on TanDEM-X, a formation-flying satellite mission performing Earth observation using interferometric Synthetic Aperture Radar (SAR) to create a Digital Elevation Model (DEM). The TanDEM-X satellite was launched as an extension joining its twin, TerraSAR-X and both satellites are operated by the German Aerospace Center (DLR). Data is managed and distributed by the European Space Agency (ESA), and the satellites were built by Airbus Defense and Space [1].

#### 1.1.b Mission Objectives

The primary goal of the mission is to create high-precision 3-dimensional models of the Earth's surface to the High-Resolution Terrain Elevation Level 3 (HRTE-3) model specification as defined by the National Geospatial Agency. Images produced by the SAR instruments aid monitoring of land and coastal processes including vegetation, glacial melt, and ocean currents. With the capability of collecting global data across the poles, this mission is critical for a range of science, government, military, and commercial applications. The secondary objective of TanDEM-X is to demonstrate novel SAR techniques in flight (including digital beamforming, along-track interferometry with a varying baseline, and super-resolution). This mission demonstrates a new orbit concept allowing for safe formation flying at close proximity between the two spacecraft [1].

Prior to TanDEM-X, DEMs have lacked full global coverage and precision required for modern navigation, military operations, and scientific applications [2]. As shown in Table 2, the novel DEM standard generated by TanDEM-X (HRTI-3) compared to the previous state-of-the-art (DTED-2) is significantly more accurate across the board, and provides spatial resolution that is sharper by more than a factor of 2.

Table 2: Comparison of DTED-2 and HRTE-3 specifications [2]

Requirement	Specification	DTED-2	HRTI-3
Relative Vertical Accuracy	90% linear point-to-point error over a $1^\circ \times 1^\circ$ cell	12 m (slope < 20%) 15 m (slope > 20%)	2 m (slope < 20%) 4 m (slope > 20%)
Absolute Vertical Accuracy	90% linear error	18 m	10 m
Relative Horizontal Accuracy	90% circular error	15 m	3 m
Horizontal Accuracy	90% circular error	23 m	10 m
Spatial Resolution	independent pixels	30 m (1 arc sec @ equator)	12 m (0.4 arc sec @ equator)

### 1.1.c Spacecraft Specification

The mission relies on formation flying involving the TanDEM-X (TDX) and TerraSAR-X (TSX) satellites. The two satellites are nearly identical and are equipped with identical X-band SAR instruments to collect high-resolution Earth images as shown by Figure 1. The main difference is that TanDEM-X features an inter-satellite S-band receiver which it uses to receive status and GPS information from TerraSAR-X. It also has been upgraded with an advanced cold-gas propulsion system for fine formation-keeping maneuvers [1] [2].

TerraSAR-X has a wet mass of 1230 kg (of which 78 kg are propellant) and have dimensions of 5m x 2.4 m. While TanDEM-X has the same dimensions, it is heavier at 1340 wet mass (of which 120 kg are propellant). The SAR antennae have dimensions of 5 m x 0.8 m and the average spacecraft power is 800 W [1] [3].

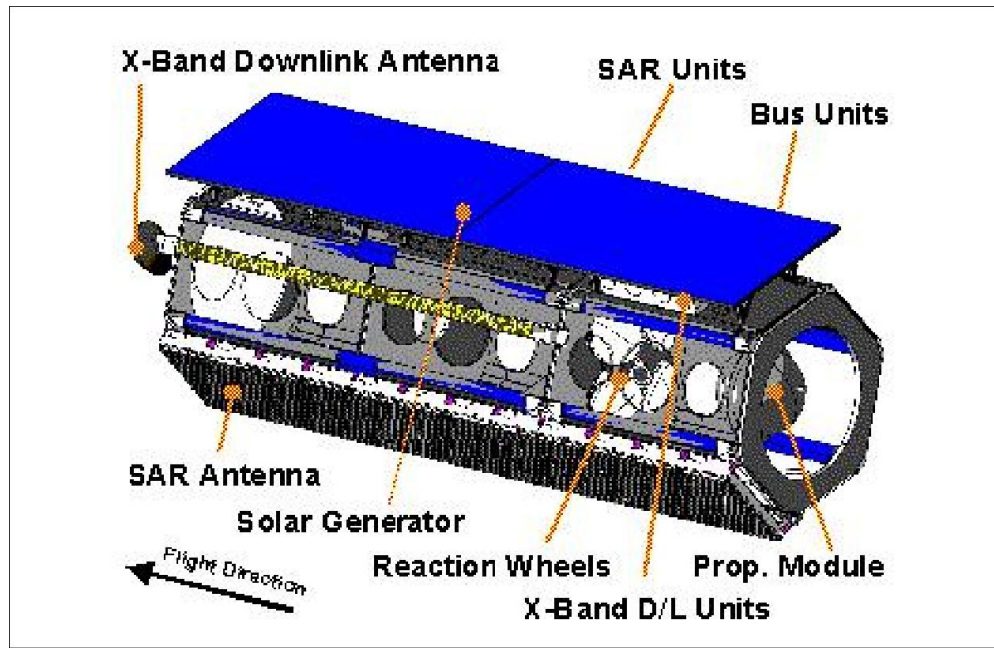


Figure 1: TerraSAR-X spacecraft features. [3]

### 1.1.d Launch and Orbit

TerraSAR-X remains in the sun-synchronous dawn-dusk circular orbit at which it was launched. Its orbit is described by a mean altitude of 514.8 km (between 505-533 km), an inclination of 97.44° and a local equator crossing time of 18:00 on the ascending node with a nominal revisit period of 11 days (and 167 orbits in the repeat) [1] [3]. The satellite was launched on June 15, 2007 from Baikonur Cosmodrome, Kazakhstan. The mission was designed for 5 years with a goal of a 6.5-year design life. As of January 2022, TerraSAR-X is still performing scientific operations in space [1].

The TanDEM-X spacecraft was launched in June 21, 2010 from Baikonur. Given the close formation with TerraSAR-X as required by the SAR mission, it is of no surprise that TanDEM-X has a practically identical orbit. To set up an effective baseline, TanDEM-X is separated in the right ascension of the ascending node with a small offset in eccentricity. A horizontal baseline between the two spacecraft is

maintained between 200 and 3000 m, depending on DEM generation requirements at different latitudes.

The relative orbits of the two spacecraft is known as a Helix formation, which allows for relatively small distances between the satellites throughout the absolute orbits while minimizing risk of collision at the poles as depicted in Figure 2. This is achieved by combining out-of-plane displacement through different ascending nodes (e.g.  $\Delta\Omega = \{300m, 400m, 500m\}$ ) and radial separation through different eccentricity vectors (e.g  $\Delta e = \{300m, 500m\}$ ). In the Helix formation, there are no crossings between the two orbits, so arbitrary along-track shifts in the orbits can be performed to finely adjust the baseline [1]. The implication of this formation is that maximum radial separation is achieved at the poles and maximum normal separation at the equator.

TanDEM-X was designed with a mission life of 5 years, and as of January 2022 is still providing SAR imagery after 12 years in orbit [1]. Both TanDEM-X and TerraSAR-X are loaded with enough fuel to continue their mission until 2026 [1].

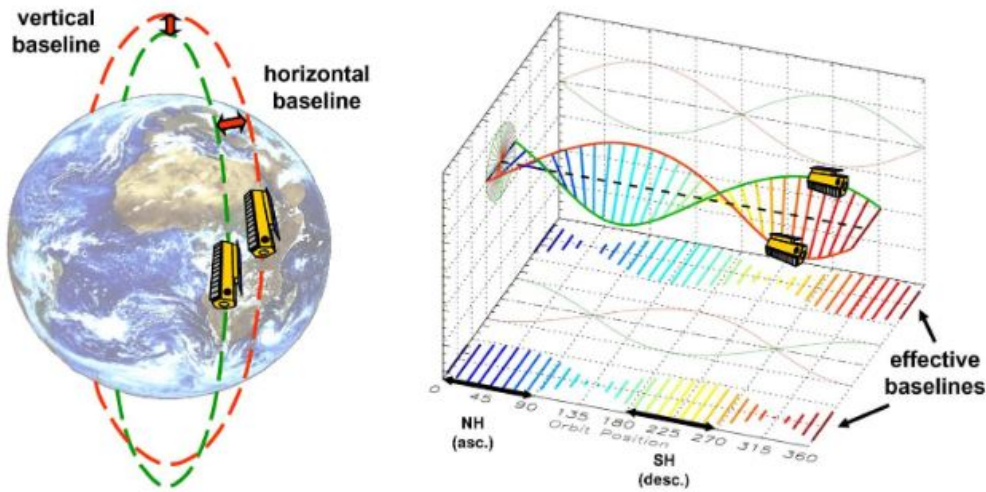


Figure 2: Helix satellite formation of TerraSAR-X and TanDEM-X illustrating relative orbits (left) and cross-track baselines as a function of orbit position (right). [2]

### 1.1.e Synthetic Aperture Radar Payload

The scientific basis of this mission is Synthetic Aperture Radar (SAR), a method of active remote sensing operable during the day, at night, and even through cloud coverage. The technology works by broadcasting a radar signal to the Earth and picking up the reflections. Comparing the reflected signal with the broadcast reveals the nature of the reflector, whether land, water, snow, ice, or otherwise [4]. In the case of TerraSAR-X and TanDEM-X, interferometric SAR can be conducted in four configurations: bistatic, monostatic, alternating bistatic, and simultaneous transmit as described in [2]. A visualization of three of these modes is shown in Figure 3.

- *Bistatic:* This mode is used to generate the DEM. One of the satellites acts as a transmitter over a common radar footprint. Both satellites collect the reflected signals and comparison of the difference generates the DEM.
- *Monostatic:* This mode has the satellites acting independently, allowing operators to skip the difficult synchronization process. With a relatively long baseline ( $\sim 10$  km), this mode is meant as a

backup in case synchronization is not feasible and generates a lower accuracy DEM.

- *Alternating bistatic*: This is similar to the bistatic mode, except that the transmitter is switched at every pulse. This mode is used to calibrate the bistatic SAR interferometer.
- *Simultaneous transmit*: In this mode, both spacecraft transmit at the same time, but the spacecraft maintain a close baseline. This mode allows for accurate synchronization and further calibration of the SAR instrument at the cost of lower range resolution for each individual image.

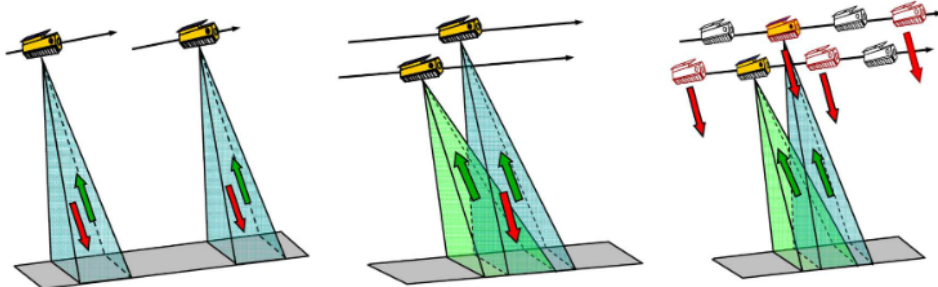


Figure 3: Data acquisition modes: Monostatic (left), bistatic (middle), and alternating bistatic (right). [2]

### 1.1.f Key Dynamics, Guidance, Navigation & Control Requirements

For SAR data collection, close-proximity formation-flying while maintaining relative separation is mission-critical. To conduct bistatic interferometry, the satellites must be maintained within a tube 250 m in radius for the duration of the mission [1]. Separation in eccentricity and ascending node is also critical to keep the two satellites in Helix formation and to maximize safety. Radial and normal separation shall not be simultaneously zero to avoid collision.

Furthermore, certain SAR techniques require tight formation-keeping and localization. Station-keeping thrusters on TanDEM-X regularly fire to counteract drift associated with J2 perturbation. At specific locations of interest, osculating along-track separations must be sufficiently precise to perform along-track interferometry.

Both spacecraft employ GPS, with TerraSAR-X demonstrating an absolute navigational accuracy of 5 cm [1]. The relative baseline between them, which is typically between 500 and 1500 km, has a 1-mm accuracy requirement in order to achieve high-precision DEM [1]. Relative control accuracy requirements are 28 m in cross-track and 200 m in along-track directions, which TanDEM-X has significantly surpassed with nominal accuracies of 5 m in cross-track and 30 m in along-track [1].

## 1.2 Problem 2: Orbit Simulation, Review of Astrodynamics

### 1.2.a Initial Orbital Elements

Given the close formation of the two spacecraft, the initial conditions are chosen to be the same orbit for the purposes of this exercise. We pick the initial conditions from TSX, which was launched on June 15, 2007 into a sun-synchronous orbit with a mean altitude of 514.8 km and inclination of 97.44°. This orbit has a local equator crossing time of 18:00 on the ascending node and was launched on the summer solstice,

corresponding to a right ascension of the ascending node (RAAN) of  $\Omega = 270^\circ$ . The nominal revisit period is 11 days (and 167 orbits in the repeat). The orbit is circular, corresponding to an eccentricity  $e = 0$ . The initial conditions can be described using the classical Keplerian orbital elements semimajor axis  $a$ , inclination  $i$ , eccentricity  $e$ , argument of periapsis  $\omega$ , RAAN  $\Omega$ , and true anomaly  $f$ :

$$\begin{aligned} a &= 6892.927 \text{ km} & \omega &= 0^\circ \\ i &= 97.44^\circ & \Omega &= 270^\circ \\ e &= 0 & f &= 0^\circ \end{aligned}$$

The argument of periapsis, and the true anomaly are not well defined for circular inclined orbits though. Additionally, having eccentricity equal to 0 can create numerical instability in code (and orbits are never perfectly circular anyways). Because of these reasons, we choose to model the following set of orbital elements instead of the classical set:

$$\begin{aligned} a &= 6892.927 \text{ km} & i &= 97.44^\circ \\ \Omega &= 270^\circ & u &= 0^\circ \\ e_x &= 1 \times 10^{-4} & e_y &= 1 \times 10^{-4} \end{aligned}$$

Note that we have chosen the argument of latitude  $u = \omega + f$  and the components of the eccentricity vector  $e = \sqrt{e_x^2 + e_y^2}$  to replace  $\omega, f, e$ . Additionally, since the location of the periapsis is undefined for circular orbits such as this one, we propose that the behaviour of the argument of latitude is similar to the true anomaly, since we can set the argument of periapsis to be arbitrarily 0, and get  $u = f$ .

### 1.2.b Initial Position and Velocity

As this is an Earth-centered satellite mission, the inertial reference frame of choice will be Earth Centered Inertial (ECI). The initial Keplerian orbital elements are converted to position and velocity in the ECI frame by first expressing them in the perifocal frame and then performing three coordinate rotations (3-1-3 Euler sequence) about each axis by the right ascension of the ascending node, inclination, and argument of periapsis. In the perifocal frame, position and velocity are given by:

$${}^P\vec{r} = \frac{a(1 - e^2)}{1 + e \cos u} \begin{bmatrix} \cos u \\ \sin u \\ 0 \end{bmatrix} \quad (1)$$

$${}^P\vec{v} = \sqrt{\frac{\mu}{a(1 - e^2)}} \begin{bmatrix} -\sin u \\ e + \cos u \\ 0 \end{bmatrix} \quad (2)$$

The transformation matrix from the perifocal to the ECI frame is given by the following, where  $R_k(\theta)$  represents the direction cosine matrix rotating about the  $k$ -axis by an angle  $\theta$ :

$$R_{PQW}^{ECI} = R_z(-\Omega)R_x(-i) \quad (3)$$

From these equations, the initial position and velocity in the ECI frame is found to be:

$$\begin{aligned} {}^I\vec{r}_{0,ECI} &= [0 \quad -6892.9 \quad 0] \text{ km} \\ {}^I\vec{v}_{0,ECI} &= [-0.9848 \quad 0 \quad 7.542] \text{ km/s} \end{aligned}$$

### 1.2.c Unperturbed and J2 Propagation Numerical Simulations

The orbit tracks shown in Figure 4 show a circular orbit under unperturbed and perturbed propagation. Introducing J2 perturbations causes a nodal precession of the orbit due to the non-spherical mass distribution of the Earth. The J2 acceleration is expressed in ECI by [5]:

$$ECI \ a_{J2} = \frac{3J_2\mu R_E^2}{2\|\vec{r}\|^5} \left[ (5\frac{r_k^2}{\|\vec{r}\|^2} - 1)(r_i\hat{I} + r_j\hat{J}) + (5\frac{r_k^2}{\|\vec{r}\|^2} - 3)r_k\hat{K} \right] \quad (4)$$

This was applied as a disturbing force  $\vec{d}$  to the 2-body differential equations of motion, which was subsequently solved by numerical integration using MATLAB *ode45*.

$$\ddot{\vec{r}} + \frac{\mu\vec{r}}{r^3} = \vec{d} \quad (5)$$

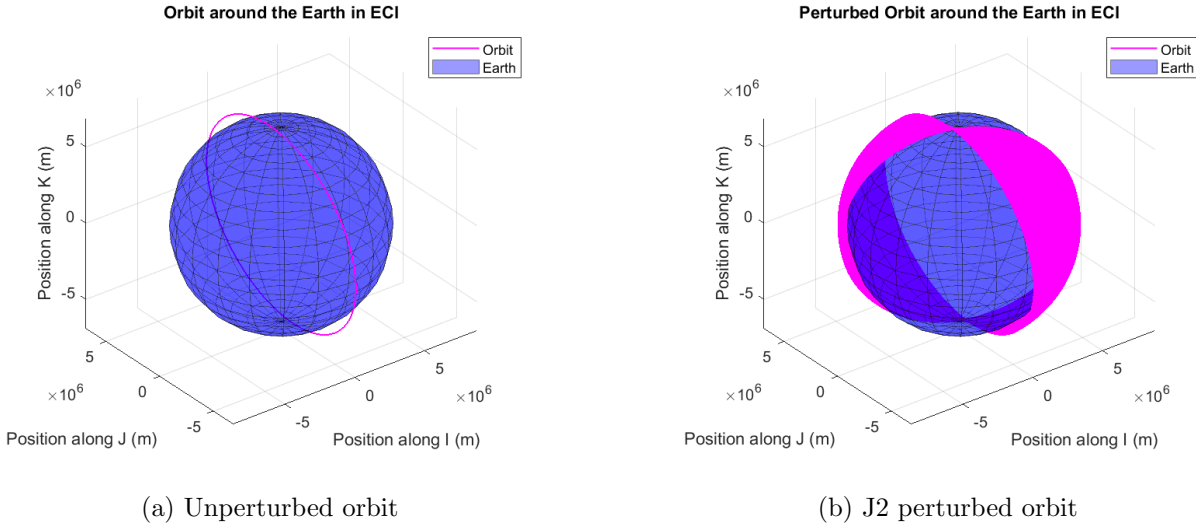


Figure 4: Simulated TDS orbital path starting on 15 June 2007 (1000 orbits).

### 1.2.d Unperturbed Numerical and Analytical Comparison

In the restricted two-body problem, the sole parameter varying with time is the mean anomaly  $M$ , which is related to the eccentric anomaly  $E$  by

$$M = \sqrt{\frac{\mu}{a^3}}(t - t_0) = E - e \sin E \quad (6)$$

The argument of latitude is related to the eccentric anomaly in the same way as the true anomaly for circular orbits

$$\tan \frac{E}{2} = \sqrt{\frac{1-e}{1+e}} \tan \frac{u}{2} \quad (7)$$

Using the same time steps as the numerical integration, Keplerian propagation was determined analytically by incrementing the mean anomaly, transforming mean anomaly into true anomaly, and applying the conic section equations (Eqs. 1 and 2) to resolve the position and velocity in the perifocal frame. With our previously validated code to transform orbital elements to the ECI frame, position and velocity were transformed from perifocal to ECI.

The position vector can be expressed in the Radial, Along-Track, and Cross-Track (RTN) frame by combining the rotation matrix  $R_{PQW}^{ECI}$  from Eq. 3 with a subsequent rotation by the argument of latitude:

$$R_{ECI}^{RTN} = R_{PQW}^{ECI} R_z(-u) \quad (8)$$

$$\vec{r}_{RTN} = R_{ECI}^{RTN} \vec{r}_{ECI} \quad (9)$$

Because the RTN frame is a non-inertial reference frame, the Theorem of Coriolis must be applied to express the velocity in RTN in addition to the coordinate transformation:

$${}^{ECI}\vec{v}_{ECI} = R_{RTN}^{ECI} \left[ {}^{RTN}\vec{v}_{RTN} + \vec{\omega}_{ECI}^{RTN} \times \vec{r}_{RTN} \right] \quad (10)$$

$${}^{RTN}\vec{v}_{RTN} = (R_{RTN}^{ECI})^T {}^{ECI}\vec{v}_{ECI} - \vec{\omega}_{ECI}^{RTN} \times \vec{r}_{RTN} \quad (11)$$

where the angular velocity of the ECI frame with respect to the RTN frame as expressed in the ECI frame is simply the rate of change of the argument of latitude:

$$\vec{\omega}_{ECI}^{RTN} = [0, 0, \dot{u}]^T$$

Plotting the absolute error between the numerical and analytical solutions as shown in Figure 5, we can see that the position error grows to the order of millimeters and the velocity error grows to the order of micrometers per second after ten orbits. These results were obtained using a tolerance of  $10^{-12}$  for the *ode45* solver and a step size of one-hundredth of the orbital period. As expected, increasing either of these two metrics led to an increase in error.

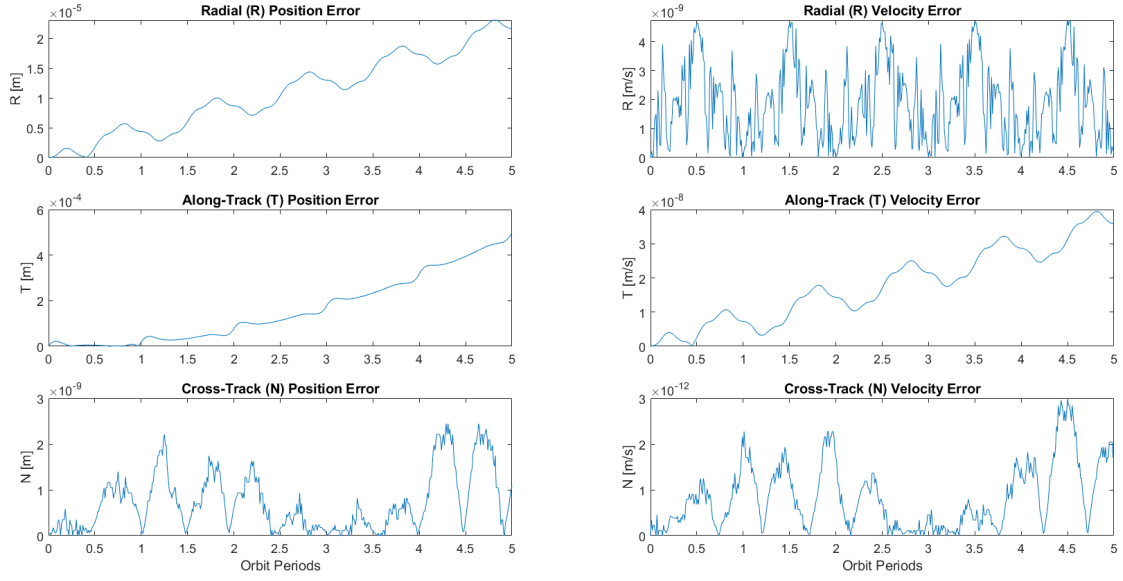


Figure 5: Absolute position and velocity errors of the numerical integration with respect to the analytical solution in the RTN frame.

### 1.2.e Osculating Orbital Elements from Numerical Simulation

Here we take the steps described in Vallado [6]. The implementation begins by constructing three vectors which define typical orbits (specific angular momentum  $\vec{h}$ , line of nodes  $\hat{n}$ , and line of apsides  $\hat{e}$ ):

$$\overset{ECI}{\vec{h}} = \overset{ECI}{\vec{r}} \times \overset{ECI}{\vec{v}} \quad (12)$$

$$\overset{ECI}{\hat{n}} = \hat{K} \times \overset{ECI}{\vec{h}} \quad (13)$$

$$\overset{ECI}{\hat{e}} = \frac{1}{\mu} \left[ \left( \left\| \overset{ECI}{\vec{v}} \right\|^2 - \frac{\mu}{\left\| \overset{ECI}{\vec{r}} \right\|} \right) \overset{ECI}{\vec{r}} - \left( \overset{ECI}{\vec{r}} \cdot \overset{ECI}{\vec{v}} \right) \overset{ECI}{\vec{v}} \right] \quad (14)$$

We can also compute the orbit shape (assuming non-parabolic) by the specific mechanical energy  $\epsilon$  and semimajor axis  $a$ :

$$\epsilon = \frac{\left\| \overset{ECI}{\vec{v}} \right\|^2}{2} - \frac{\mu}{\left\| \overset{ECI}{\vec{r}} \right\|} \quad (15)$$

$$a = -\frac{\mu}{2\epsilon} \quad (16)$$

We finally find the orientation of the orbit:

$$i = \cos^{-1} \left( \frac{h_K}{\left\| \overset{ECI}{\vec{h}} \right\|} \right) \quad (17)$$

$$\Omega = \cos^{-1} \left( \frac{n_I}{\|ECI \hat{n}\|} \right) \quad (18)$$

$$u = \cos^{-1} \left( \frac{ECI \hat{n} \cdot ECI \vec{r}}{\|ECI \hat{n}\| \|ECI \vec{r}\|} \right) \quad (19)$$

In addition, checks in the code are performed to ensure that these angles are evaluated in the correct quadrants within the range  $[0, 2\pi]$ .

The orbital elements, specific angular momentum, and specific energy are plotted for simulations including and excluding J2 effects in Figure 6. For unperturbed orbit propagation, all orbital elements are constant except for the argument of latitude ( $u$ ) as the satellite propagates its orbit. Additionally, the line of apsides defined by the vector  $e$  is constant while the specific angular momentum changes slightly in the  $\hat{K}$  component as shown in Figure 7. Over a period of 5 orbits, this variance was calculated to be on the order of  $1m^2/s$ , which is significantly smaller than the magnitude of specific angular momentum ( $10^{10} m^2/s$ ). This discrepancy may be attributed to numerical integration errors.

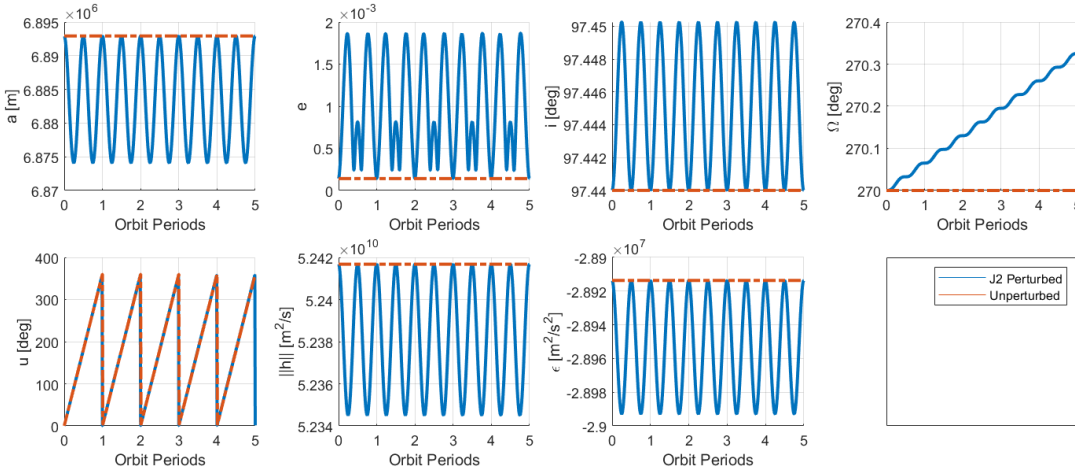


Figure 6: Orbital elements, specific angular momentum, and specific energy over 5 orbits for J2 (blue) and unperturbed (red) propagation.

Including J2 effects (short and long period oscillations), we find that all orbital elements, the specific mechanical energy, the line of apsides and the specific angular momentum exhibit periodicity. The right ascension of the ascending node  $\Omega$  is clearly under secular effects as is expected for an inclined orbit due to precession. Likewise, we observe that the specific angular momentum demonstrates secular effects along the  $\hat{J}$  and  $\hat{K}$  directions, which is also to be expected due to the changes in RAAN.

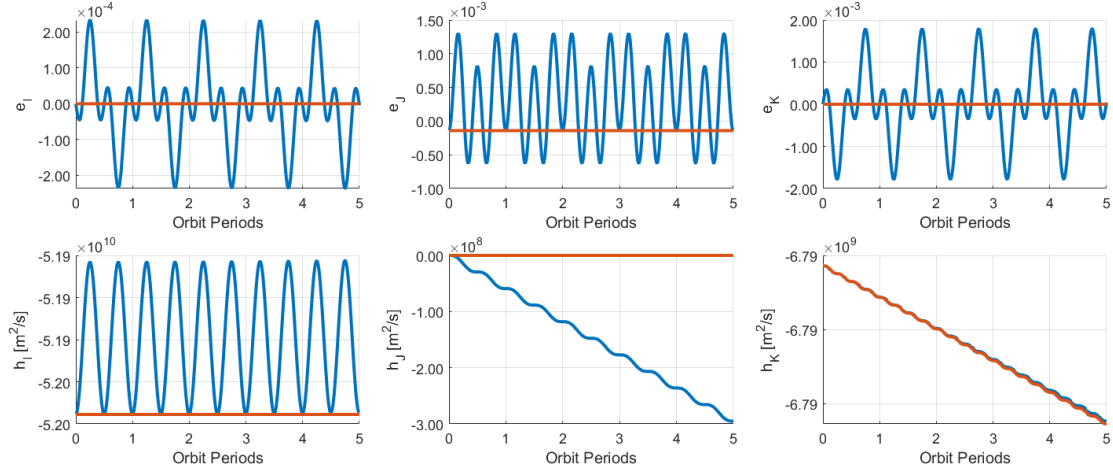


Figure 7: Line of apsides and specific angular momentum over 5 orbits for J2 (blue) and unperturbed (red) propagation.

### 1.2.f Mean Classical Orbital Elements

The differential equations for the mean classical orbital elements reflect zero variations in  $a$ ,  $e$ , and  $i$  over time. The following linear differential equations are used in order to update the new state composed of orbital elements [7]:

$$\frac{d\Omega}{dt} = -\frac{3}{2}nJ_2 \left( \frac{R_E}{p} \right)^2 \cos(i) \quad (20)$$

$$\frac{du}{dt} = \frac{3}{4}nJ_2 \left( \frac{R_E}{a(1-(e_x^2+e_y^2))} \right)^2 \left( \sqrt{1-(e_x^2+e_y^2)}(3\cos^2 i - 1) + (5\cos^2 i - 1) \right) \quad (21)$$

$$\frac{de_x}{dt} = -\frac{3}{4}nJ_2 \left( \frac{R_E}{a(1-(e_x^2+e_y^2))} \right)^2 e_y (5\cos^2 i - 1) \quad (22)$$

$$\frac{de_y}{dt} = \frac{3}{4}nJ_2 \left( \frac{R_E}{a(1-(e_x^2+e_y^2))} \right)^2 e_x (5\cos^2 i - 1) \quad (23)$$

We follow a similar procedure as in the previous section to produce an evolution of the state vector across 5 orbits. Superimposing the resulting mean orbital elements, specific angular momentum, and specific energy with their osculating values in Figure 8 and Figure 9 shows they are generally in agreement.

Under averaging theory, we know the J2 perturbs the right ascension of the ascending node, the argument of periapsis and the mean anomaly. Since we are using the argument of latitude, the effects of the latter two get folded into this one. We see this clearly in Figure 8, where the only secular effects are observed in the right ascension of the ascending node. Although the argument of latitude appears to be unperturbed, taking a closer look at the region in Figure 10 shows that the values are slightly precessing. Note that this precession is due to  $J_2$ , and that under the averaging theory we ignore motion that is periodic. This is why, unlike in the propagation of the position and velocity state vector, we do not see rapid changes in the argument of latitude as the satellites traverses its orbit.

Additionally, given the equations above, we would not expect a perfectly circular orbit to have any effects on its eccentricity by  $J_2$ . In Figure 10, we do see very slight changes, and this is likely a numerical error.

When we calculate the initial eccentricity vector we arrive at a practically 0 value, but due to slight numerical error it is not exactly 0.

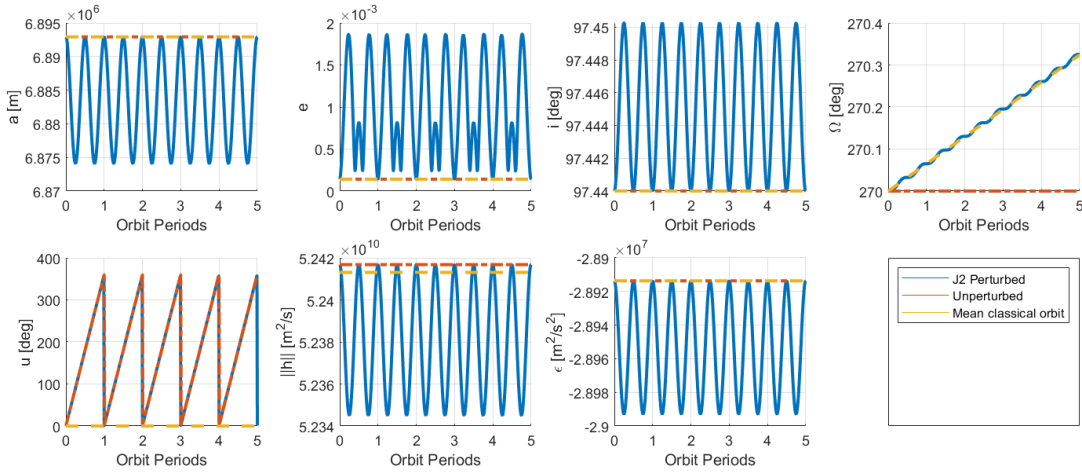


Figure 8: Orbital elements, specific angular momentum, and specific energy over 5 orbits for J2 (blue), unperturbed (red), and mean classical (yellow) orbit propagation.

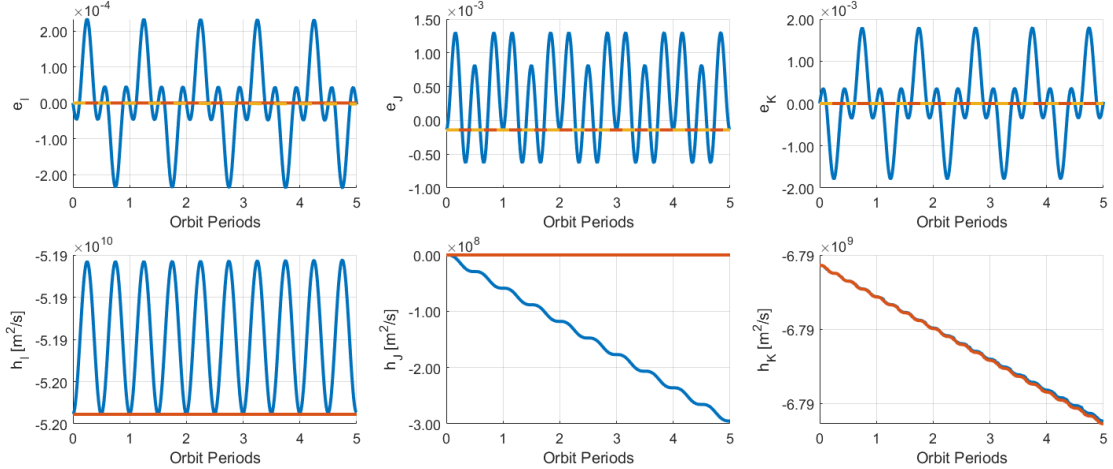


Figure 9: Line of apsides and specific angular momentum over 5 orbits for J2 (blue), unperturbed (red), and mean classical (yellow) orbit propagation.

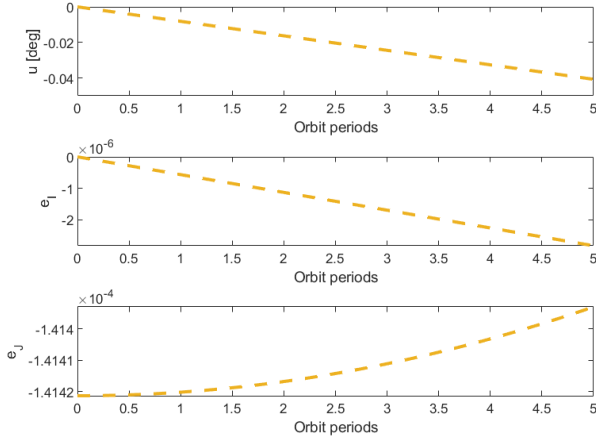


Figure 10: Isolating seemingly unperturbed parameters of the mean classical orbit propagation reveals small precession.

### 1.2.g Reconciling Osculating and Mean Orbital Elements

Inconsistencies during initialization can be mitigated using Brouwer theory to transform between mean and osculating values. We see this issue when comparing the unperturbed and the mean orbital elements of RAAN and argument of latitude  $u$ . Applying Brouwer theory would allow us to better match the behaviour of the mean classical orbit case in Figure 8 with the behaviour seen in the J2 perturbed case.

## 2 Problem Set 2

### 2.1 Problem 1: Everything is Relative

#### 2.1.a Chief and Deputy Orbit Initialization

Non-singular orbit elements will be used since the TSX satellite flies in a circular orbit. TSX is selected as the chief orbit with TDX as its deputy. In this case, TDX employs e/i vector separation in order to have a safe orbit that avoids crossing paths with TSX. We will be modeling the first phase of the mission (preliminary DEM generation), reported with the following difference in eccentricity  $a\delta e$ , difference in inclination  $a\delta i$ , and difference in phase angle [8]:

$$a\delta e = 260 \text{ m}, \quad a\delta i = 222 \text{ m}, \quad \theta - \phi = 200^\circ$$

These offsets are transformed to the orbital elements used in this project using polar coordinates. The subscript 0 refers to the chief orbit and the subscript 1 refers to the deputy orbit.

$$\Delta e = \begin{bmatrix} \Delta e_x \\ \Delta e_y \end{bmatrix} = \delta e \begin{bmatrix} \cos(\phi) \\ \sin(\phi) \end{bmatrix} \quad (24)$$

$$\Delta i = \begin{bmatrix} \Delta i_x \\ \Delta i_y \end{bmatrix} = \delta i \begin{bmatrix} \cos(\theta) \\ \sin(\theta) \end{bmatrix} = \begin{bmatrix} i_1 - i_0 \\ (\Omega_1 - \Omega_0)\sin(i_0) \end{bmatrix} \quad (25)$$

Using these relations, the relative eccentricity and inclination of the chief and deputy may be determined. We design the phase angle  $\theta = +45^\circ$ , the argument of latitude in which the deputy crosses the orbital plane of the chief, in order to produce a safe relative orbit as will be shown. The initial conditions for this leader and follower setup are given in Table 3.

	$a$	$e_x$	$e_y$	$i$	$\Omega$	$u$
TSX	6892.927 km	$1 \times 10^{-4}$	$1 \times 10^{-4}$	$97.44^\circ$	$270^\circ$	$0^\circ$
TDX	6892.927 km	$6.5814 \times 10^{-5}$	$8.4059 \times 10^{-5}$	$97.4413^\circ$	$270.0013^\circ$	$0^\circ$

Table 3: Initial orbital parameters of TSX and TDX in Helix formation.

#### 2.1.b Numerical Integration of Relative Equations of Motion

Relative motion between the chief and deputy spacecraft can be derived as a 10-dimensional system of differential equations describing the relative acceleration of the deputy in the rotating RTN frame as  $[\ddot{x}, \ddot{y}, \ddot{z}]$  and the acceleration of the chief as  $[\ddot{r}_0, \ddot{\theta}]$ . The system is represented by the state vector  $[\vec{r}, \vec{\rho}, r_0, \theta_0, \dot{r}_0, \dot{\theta}_0]$ .

$$\ddot{x} - 2\dot{\theta}_0\dot{y} - \dot{\theta}_0^2x = -\frac{\mu(r_0 + x)}{[(r_0 + x)^2 + y^2 + z^2]^{\frac{3}{2}}} + \frac{\mu}{r_0^2} \quad (26)$$

$$\ddot{y} + 2\dot{\theta}_0\dot{x} + \dot{\theta}_0^2y = -\frac{\mu y}{[(r_0 + x)^2 + y^2 + z^2]^{\frac{3}{2}}} \quad (27)$$

$$\ddot{z} = -\frac{\mu z}{[(r_0 + x)^2 + y^2 + z^2]^{\frac{3}{2}}} \quad (28)$$

$$\ddot{r}_0 = r_0 \dot{\theta}_0^2 - \frac{\mu}{r_0^2} \quad (29)$$

$$\ddot{\theta}_0 = -\frac{2\dot{r}_0 \dot{\theta}_0}{r_0} \quad (30)$$

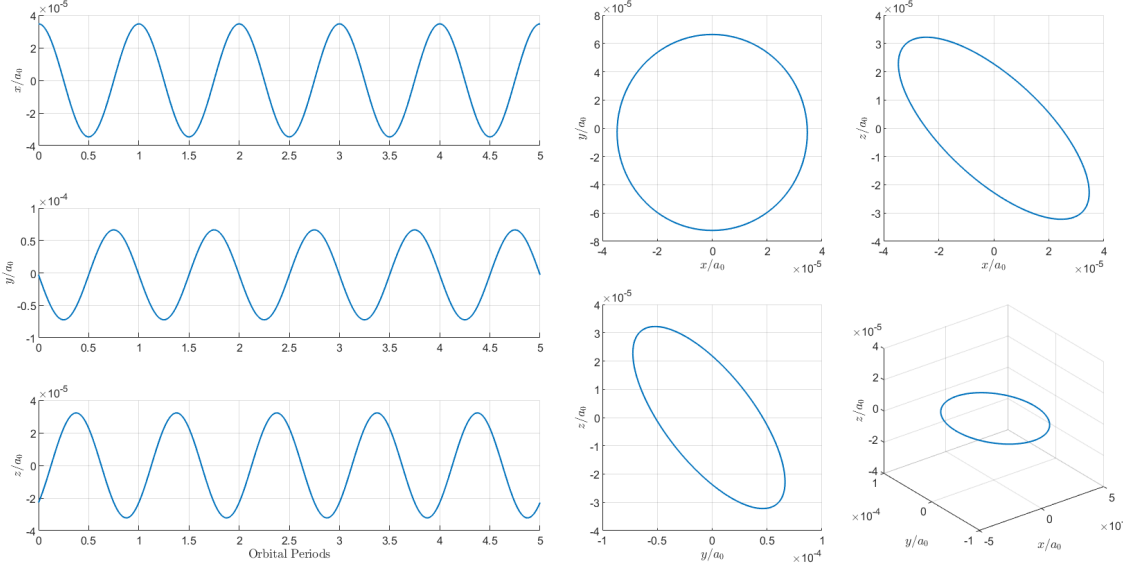


Figure 11: Numerically integrated relative RTN position of the deputy (TDX) with respect to the chief (TSX) using the non-linear equations of relative motion.

These differential equations are numerically integrated using *ode45*, and the results are shown in Figure 11 and 12. The corresponding initial conditions are found by finding the initial ECI position and velocities of the orbits from the orbital elements in part a. We then employ differences, coordinate transforms and the Theorem of Coriolis to find the correct initial conditions. The superscript 0 corresponds to the fact that these are initial conditions, while the subscript indicated the chief (0) or deputy (1). The rotation matrix and the corresponding rotation rates are taken with respect to the chief's orbit.

$$\theta_0 = u_0^0; \quad (31)$$

$$\dot{\theta}_0^0 = \sqrt{\frac{\mu}{a_0^3(1-e_0^2)^3}} \left(1 + e_0 * \cos(\theta_0)\right)^2 \quad (32)$$

$$ECI \vec{\omega}^{RTN} = [0, 0, \dot{\theta}_0^0] \quad (33)$$

$$R_{ECI}^{RTN} = R_z(-\Omega_0)R_x(-i_0)R_z(-u_0^0) \quad (34)$$

$$ECI \vec{\rho}^0 = ECI \vec{r}_1^0 - ECI \vec{r}_0^0 \quad (35)$$

$$ECI \dot{\vec{\rho}}^0 = ECI \vec{v}_1^0 - ECI \vec{v}_0^0 \quad (36)$$

$$RTN \vec{\rho}^0 = R_{ECI}^{RTN} ECI \vec{\rho}^0 \quad (37)$$

$$RTN \dot{\vec{\rho}}^0 = R_{ECI}^{RTN} ECI \dot{\vec{\rho}}^0 - ECI \vec{\omega}^{RTN} \times RTN \vec{\rho}^0 \quad (38)$$

$$RTN \vec{r}_0^0 = R_{ECI}^{RTN} ECI \vec{r}_0^0 \quad (39)$$

$$\vec{r}_0^0 = \left\| RTN \vec{r}_0^0 \right\|_2 \quad (40)$$

$$\dot{\vec{r}}_0^0 = \left\| R_{ECI}^{RTN} ECI \vec{v}_0^0 - ECI \vec{\omega}^{RTN} \times RTN \vec{r}_0^0 \right\|_2 \quad (41)$$

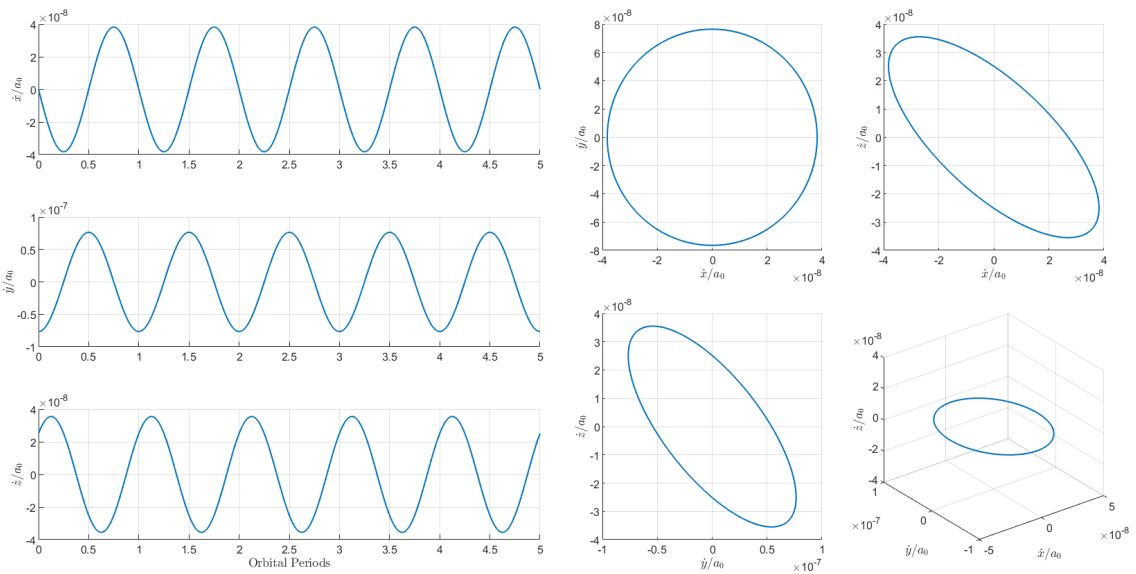


Figure 12: Numerically integrated relative RTN velocity using the non-linear equations of relative motion.

### 2.1.c Analytical Solution to Fundamental Orbital Differential Equations

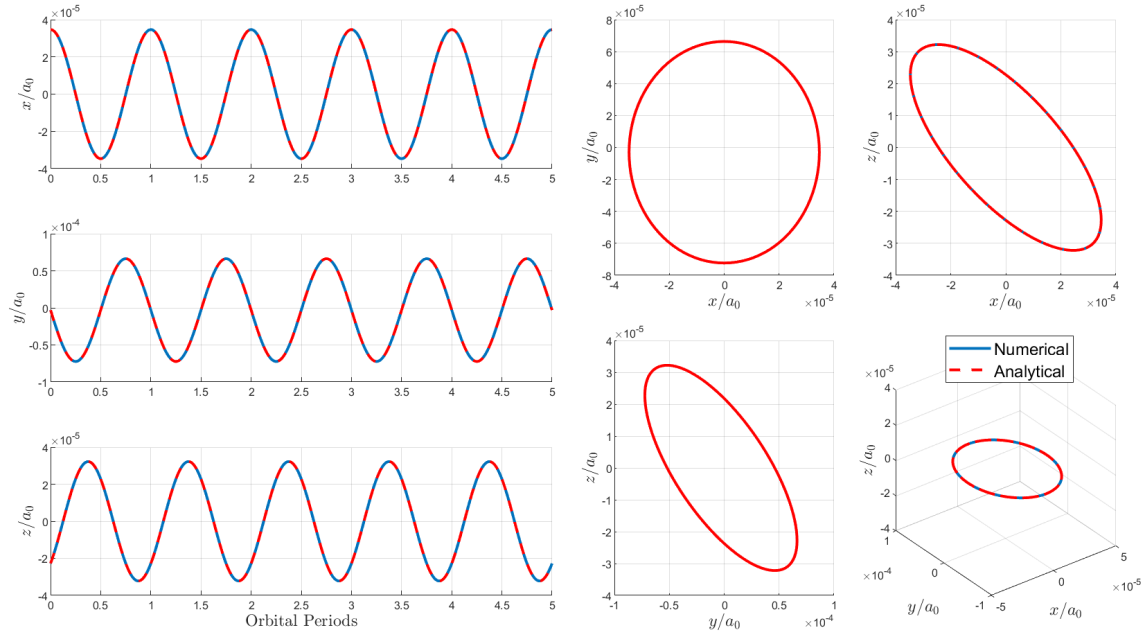


Figure 13: Overlaid numerically integrated (blue) and analytically determined (red) relative RTN position.

We choose to analytically solve for the absolute position of the chief and deputy using the fundamental orbital differential equations in order to adequately compare with the nonlinear relative equations of motion. We can then take the difference between the vectors in ECI, and perform a transformation from ECI to RTN as was done in 1.2.d. The resulting relative positions and velocities of the deputy with respect to the chief in the RTN frame is shown in Figure 13 and 14. Due to the fact that the numerical and analytical simulations show extremely small error, the position and velocity plots appear indistinguishable as they are stacked on top of one another as will be discussed in the next section.

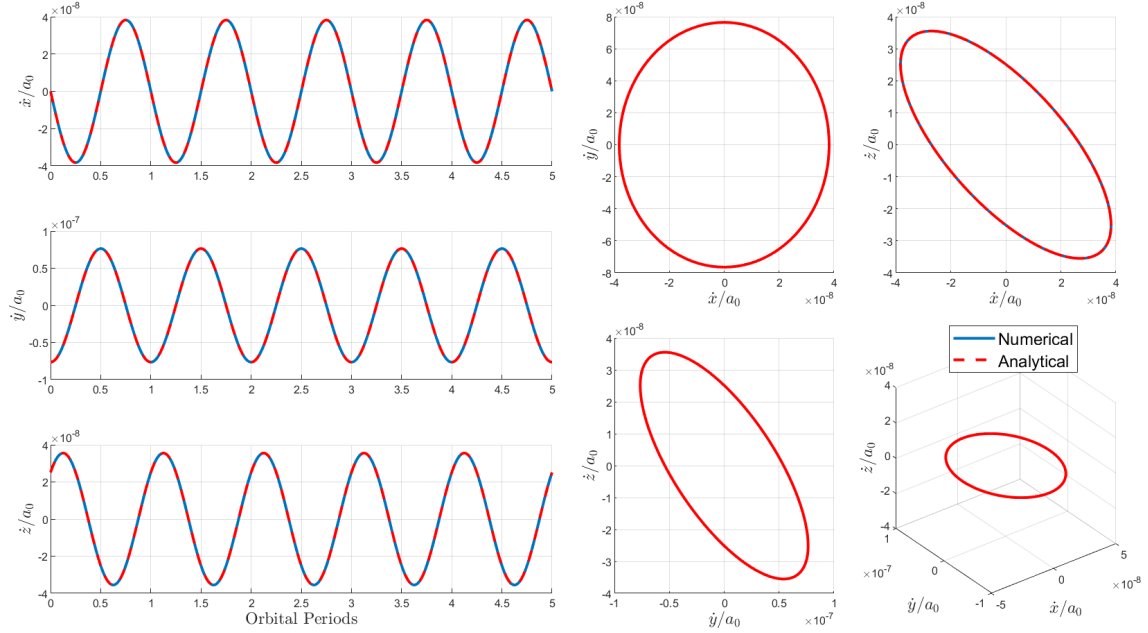


Figure 14: Overlaid numerically integrated (blue) and analytically determined (red) relative RTN velocity.

#### 2.1.d Numerical and Analytical Comparison

The relative position as found by the analytical equations exhibits periodicity in the X, Y, and Z coordinates in the RTN frame and aligns closely with that found by the nonlinear numerical integration. Numerical error between the two approaches produces the largest difference on the order of picometers ( $10^{-12}$  meters) in the along-track direction as shown in Figure 15. The error in velocity is even smaller as seen in Figure 16.

The error is similarly small for changing initial conditions when a 100-m difference is introduced in the semi-major axis. The order of magnitude in this case is also as large as  $10^{-12}$  m as can be seen in Figure 17. However, as can be observed in Figure 18, this causes an along-track drift and the relative motion is no longer bounded.

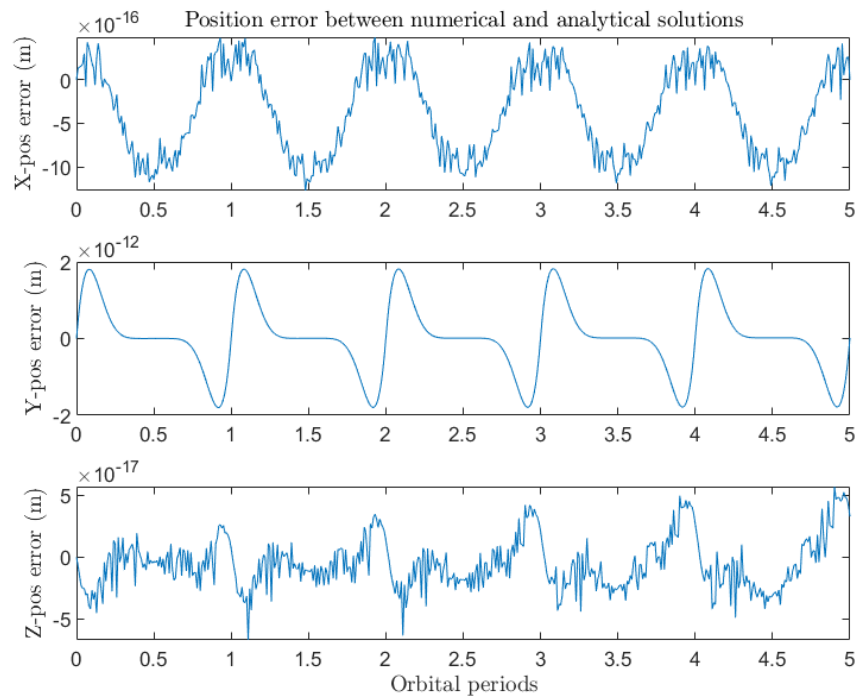


Figure 15: Position error in the RTN frame between the numerical and analytical solutions.

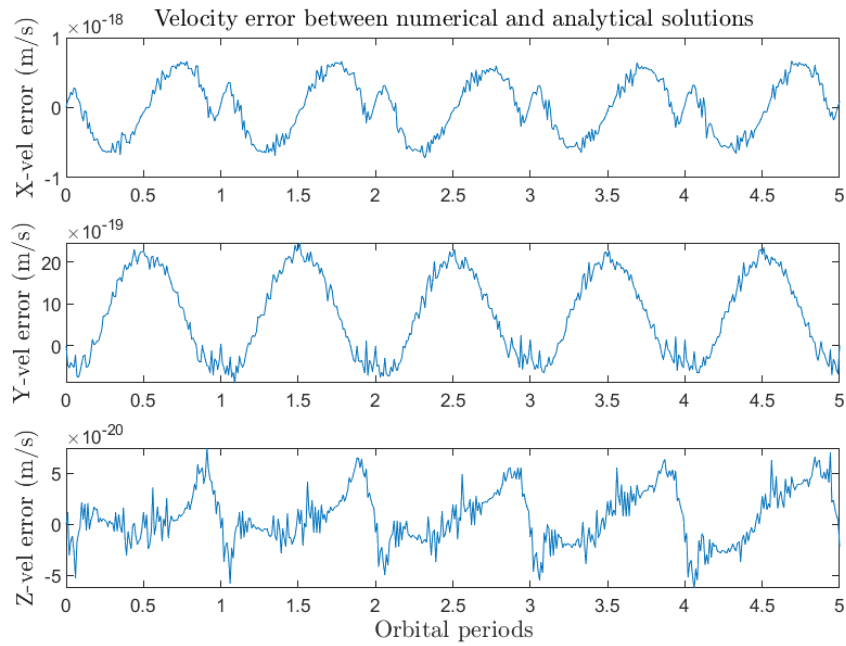


Figure 16: Velocity error in the RTN frame between the numerical and analytical solutions.

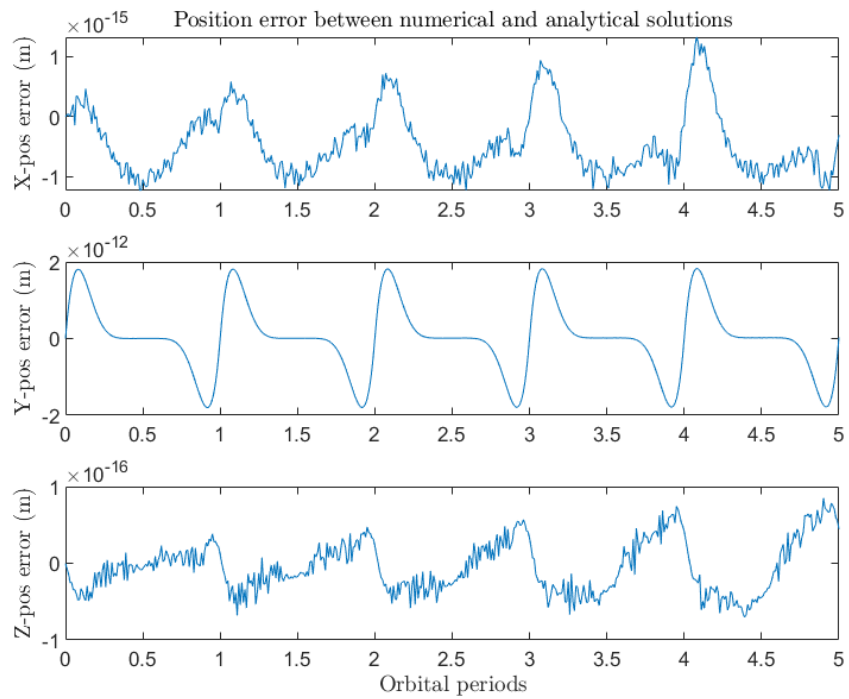


Figure 17: Position error between the numerical and analytical solutions with a difference in initial semi-major axis.

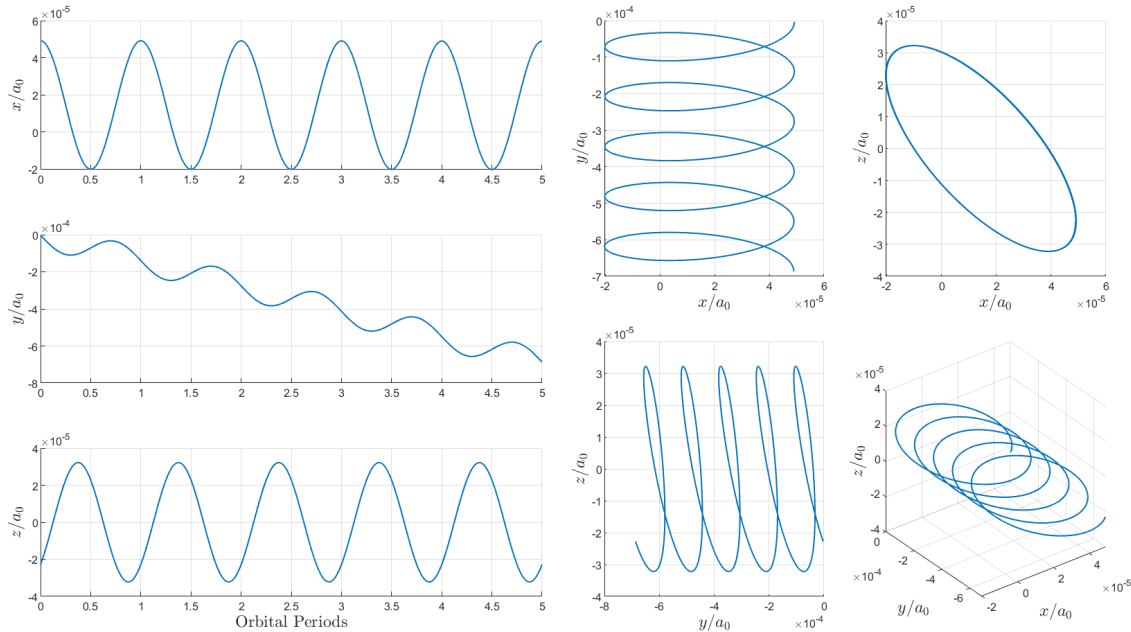


Figure 18: Numerically integrated relative RTN position with a difference in initial semi-major axis.

### 2.1.e Drift Correction Maneuver

To correct for the drift, an impulsive maneuver is executed to lower the semi-major axis by 100m and re-establish periodicity between the chief and deputy. Due to the Oberth effect, the location at which a maneuver will have the largest effect on the specific mechanical energy (and therefore require the lowest fuel) is the point of largest velocity magnitude. This occurs at the periapsis as is seen in the vis-viva equation. For perfectly circular orbits, the location of the maneuver is not as relevant since the velocity magnitude is constant – the  $\Delta v$  required does not significantly vary from one location to another. However, to be as precise as possible, we will implement this maneuver at the periapsis of the deputy's orbit since its orbit is slightly eccentric.

The required  $\Delta v$  of the maneuver can be calculated using the Gauss Variational Equations, expressed in the velocity frame in the following equations. Note that the velocity frame is equivalent to the RTN frame at periapsis.

$$\frac{da}{dt} = \frac{2a^2v}{\mu} a_v \quad (42)$$

$$\Delta a = \frac{2a^2v_p}{\mu} \Delta v_T \rightarrow \Delta v_T = \Delta a \frac{\mu}{2a^2v_p} \quad (43)$$

$$v_p = \sqrt{\mu \left( \frac{2}{r_p} - \frac{1}{a} \right)}, \quad r_p = a(1 - e) \quad (44)$$

Therefore, we will have an impulsive maneuver at periapsis in the along-track direction of:

$$\Delta v_T = -0.0552 \text{ m/s}$$

### 2.1.f Maneuver Simulation

As shown in Figure 19, the applied  $\Delta v_T$  maneuver (which was applied to change only the semi-major axis) corrects the along-track drift and restores periodic relative motion between the two spacecraft.

Since the orbit simulation begins at the periapsis, after 3 orbits the  $\Delta v_T$  is applied. This is observed as a discontinuity in the along-track velocity component at the beginning of the fourth orbit as shown in Figure 20.

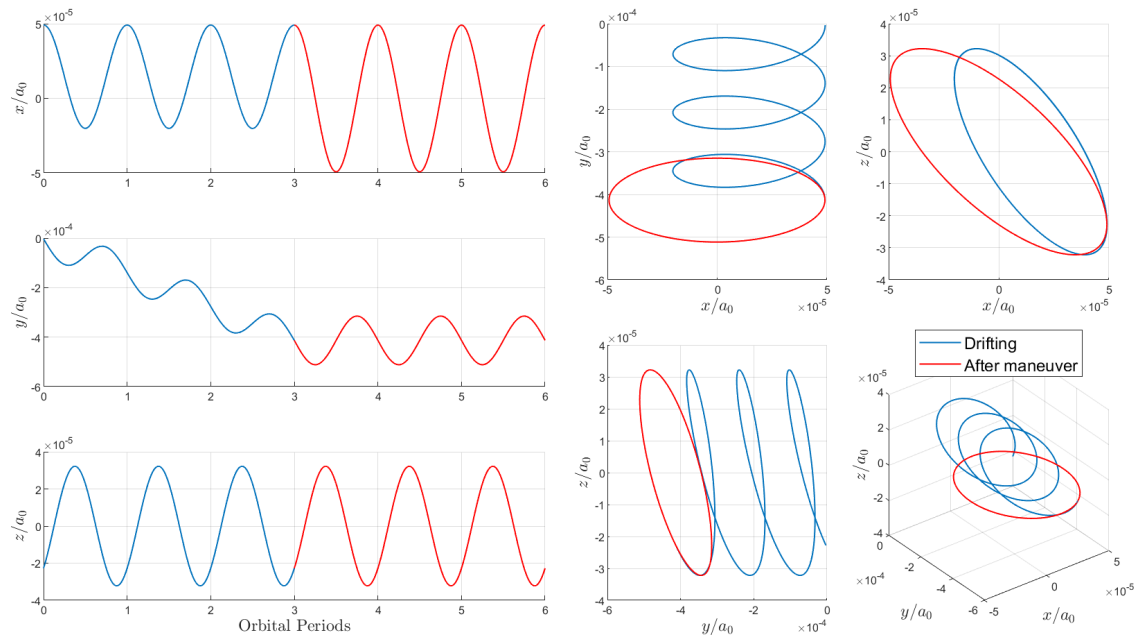


Figure 19: Numerically integrated relative RTN position before (blue) and after (red) the maneuver.

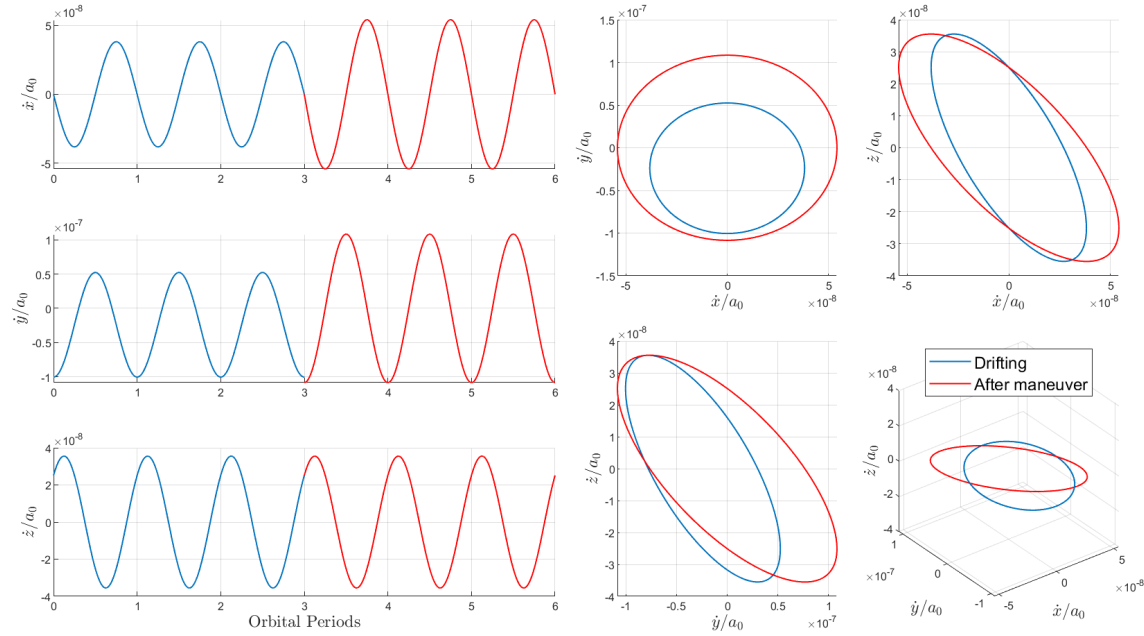


Figure 20: Numerically integrated relative RTN velocity before (blue) and after (red) the maneuver.

### 3 Problem Set 3

#### 3.1 Problem 1: We are Close in Near-Circular Orbits

##### 3.1.a Initial Conditions

The linearized equations of relative motion known as Hill-Clohessy-Wilshire (HCW) are valid for the previously defined orbit, satisfying the assumptions of small relative motion with respect to the orbit radius ( $\rho = 0.00005r_0$ ) and near-circular eccentricity ( $e_0 = 0.00014$ ,  $e_1 = 0.00011$ ). The same initial conditions as described in 2.1.a satisfy these assumptions and will be used in the following analysis.

##### 3.1.b Initial Position and Velocity

By the same procedure to convert from orbital elements as described by Eqns. 1-3, the initial positions and velocity of the chief and deputy are calculated to be:

$$\begin{aligned} {}^I\vec{r}_{0,ECI} &= [0 \quad -6892.9 \quad 0] \text{ km} \\ {}^I\vec{v}_{0,ECI} &= [-0.9848 \quad 0 \quad 7.542] \text{ km/s} \\ {}^I\vec{r}_{1,ECI} &= [158.3 \quad -6892.9 \quad 0] \text{ km} \\ {}^I\vec{v}_{1,ECI} &= [-0.9850 \quad 2.26 \times 10^{-5} \quad 7.541] \text{ km/s} \end{aligned}$$

In the chief RTN frame, relative position may be determined by a coordinate transform, and relative velocity by a coordinate transform and application of the Theorem of Coriolis as given by Eqns. 33-38.

$$\begin{aligned} {}^{RTN}\vec{\rho}_{0,RTN} &= [238.9 \quad -20.50 \quad -157.0] \text{ m} \\ {}^{RTN}\vec{\rho}_{0,RTN} &= [2.3763 \times 10^{-6} \quad -0.5273 \quad 0.1732] \text{ m/s} \end{aligned}$$

The absolute orbit elements corresponding to this motion in the inertial frame are given in Table 3. Differences in orbit elements between the chief and deputy are shown in Table 4.

$\Delta a$	$\Delta e_x$	$\Delta e_y$	$\Delta i$	$\Delta \Omega$	$\Delta u$
0	$-3.419 \times 10^{-5}$	$-1.594 \times 10^{-5}$	$2.277 \times 10^{-5}$	$2.297 \times 10^{-5}$	0

Table 4: Differences in initial orbit elements.

##### 3.1.c Hill-Clohessy-Wilshire Integration Constants

The solution to the HCW equations in matrix-vector form are expressed by:

$$\begin{bmatrix} x \\ y \\ z \\ \dot{x} \\ \dot{y} \\ \dot{z} \end{bmatrix} = \begin{bmatrix} aI_{3 \times 3} & 0_{3 \times 3} \\ 0_{3 \times 3} & anI_{3 \times 3} \end{bmatrix} \begin{bmatrix} 1 & \sin(nt) & \cos(nt) & 0 & 0 & 0 \\ -\frac{3}{2}nt & 2\cos(nt) & -2\sin(nt) & 1 & 0 & 0 \\ 0 & 0 & 0 & 0 & \sin(nt) & \cos(nt) \\ 0 & \cos(nt) & -\sin(nt) & 0 & 0 & 0 \\ -\frac{3}{2} & -2\sin(nt) & -2\cos(nt) & 0 & 0 & 0 \\ 0 & 0 & 0 & 0 & \cos(nt) & -\sin(nt) \end{bmatrix} \begin{bmatrix} K_1 \\ K_2 \\ K_3 \\ K_4 \\ K_5 \\ K_6 \end{bmatrix} \quad (45)$$

where  $n$  is defined as  $n = \sqrt{\frac{\mu}{a_0^3}}$ . Given the initial state at time  $t_0 = 0$ , the six integration constants  $K_1$  to  $K_6$  are found to be

$$\begin{bmatrix} K_1 \\ K_2 \\ K_3 \\ K_4 \\ K_5 \\ K_6 \end{bmatrix} = \begin{bmatrix} 2.927 \times 10^{-8} \\ 3.125 \times 10^{-10} \\ 3.470 \times 10^{-5} \\ -2.974 \times 10^{-6} \\ 2.278 \times 10^{-5} \\ -2.277 \times 10^{-5} \end{bmatrix}$$

### 3.1.d HCW in Rectilinear Coordinates

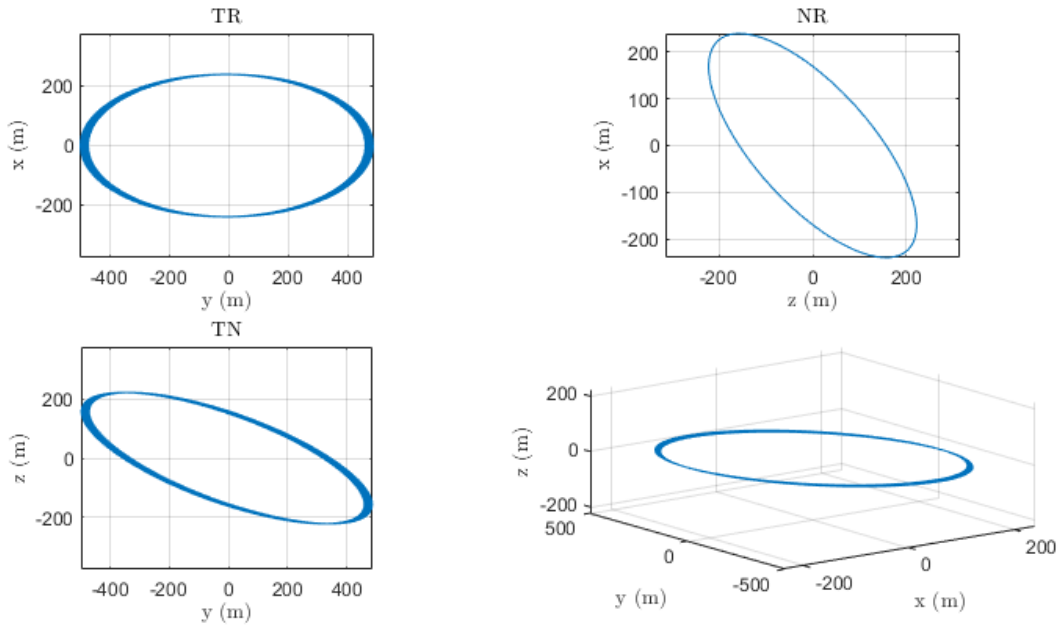


Figure 21: Numerically integrated relative RTN position from HCW equations over 15 orbits.

The homogeneous HCW equations are given by the following, assuming no disturbing or control forces:

$$\ddot{x} - 2n\dot{y} - 3n^2x = 0 \quad (46)$$

$$\ddot{y} + 2n\dot{x} = 0 \quad (47)$$

$$\ddot{z} + n^2z = 0 \quad (48)$$

Starting from the initial conditions and integrating these equations over 15 orbits, we observe that the relative motion between the chief and the deputy is periodic as shown in by the position plots in Figure 21 and the velocity plots in Figure 22. In each of the TR, NR, and TN planes, the motion of the deputy is elliptic.

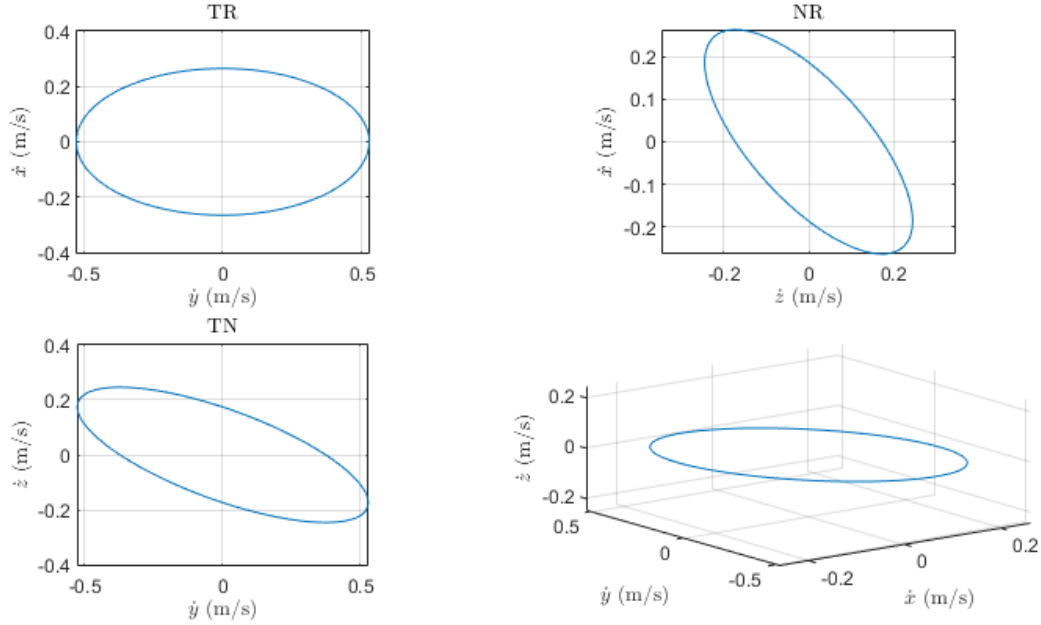


Figure 22: Numerically integrated relative RTN velocity from HCW equations over 15 orbits.

### 3.1.e HCW in Rectilinear Coordinates

With an initial difference in eccentricity and inclination but identical semi-major axes, the relative motion appears periodic as expected by the energy matching condition. The motion in the TR plane forms a 2-by-1 ellipse with semi-minor axis as a function of the integration constants given by  $a\sqrt{(K_2^2 + K_3^2)}$ . Upon inspection across 50 orbits, there is an along-track drift as shown in Figure 23. This behavior is expected from the solution to the HCW equations in which the position in  $y$  grows linearly with time. Though the energy matching condition is met, there is unbounded motion inherent in the HCW solution. This can be mitigated by setting the initial conditions such that  $\dot{y}(0) = 2nx(0)$ , driving the secular term to zero.

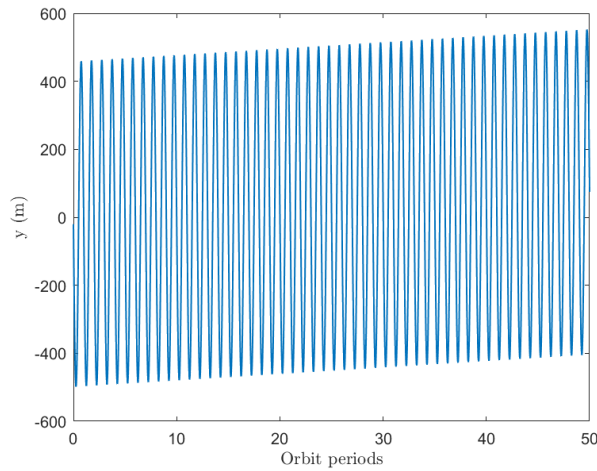


Figure 23: Along-track drift apparent in HCW solution over 50 orbits.

### 3.2 Problem 2: We are Close in Eccentric Orbits

#### 3.2.a Initial Conditions

For eccentric orbits, the Yamanaka-Ankersen solution employs true anomaly as the independent variable. Therefore, for this analysis we revert back to singular orbital elements and singular relative orbital elements. Most of the orbital elements from 2.1.a still apply, but we now re-introduce the argument of periapsis for eccentric orbits and select true anomaly as the phase angle. First, we find that an orbit with a semi-major axis of 6892.927 km as before with an eccentricity of 0.1 will have a perigee below the Earth's surface. So, we set the periapsis radius to the same as the semi-major axis from 2.1.a to calculate a new semi-major axis for this problem. The chief's absolute initial orbital parameters are:

$$\begin{aligned} a &= 7658.808 \text{ km} & i &= 97.44^\circ \\ e &= 0.1 & \omega &= 0^\circ \\ \Omega &= 270^\circ & f &= 0^\circ \end{aligned}$$

We follow a similar procedure as in 3.1.b to obtain the initial relative position and velocities in RTN:

$$\begin{aligned} {}^{RTN}\vec{\rho}_{0,RTN} &= [-260.0 \quad -18.45 \quad -141.3] \text{ m} \\ {}^{RTN}\vec{\rho}_{0,RTN} &= [4.8879 \times 10^{-6} \quad 0.5743 \quad 0.1635] \text{ m/s} \end{aligned}$$

This new set of orbital elements are set to be valid under the Tschauner-Hempel (TH) equations, satisfying small relative motion compared to the radius of periapsis ( $\rho = 0.00004r_{p0}$ ) and equal semi-major axes. The singular relative orbital parameters are given by:

$$\begin{bmatrix} \delta a \\ \delta M_0 \\ \delta e \\ \delta \omega \\ \delta i \\ \delta \Omega \end{bmatrix} = \begin{bmatrix} (a_1 - a_0)/a_0 \\ M_1 - M_0 \\ e_1 - e_0 \\ \omega_1 - \omega_0 \\ i_1 - i_0 \\ \Omega_1 - \Omega_0 \end{bmatrix} = \begin{bmatrix} 0 \\ 0 \\ 3.3948 \times 10^{-5} \\ 0 \\ 2.0496 \times 10^{-5} \\ 2.0670 \times 10^{-5} \end{bmatrix}$$

#### 3.2.b Yamanaka-Ankersen Integration Constants

The YA solution obtains the relative state at any time from a given initial state. In matrix-vector form, this can also be expressed using integration constants as given by:

$$\begin{bmatrix} x \\ y \\ z \\ \dot{x} \\ \dot{y} \\ \dot{z} \end{bmatrix} = \begin{bmatrix} a\eta^2 I_{3 \times 3} & 0_{3 \times 3} \\ 0_{3 \times 3} & \frac{an}{\eta} I_{3 \times 3} \end{bmatrix} \begin{bmatrix} \Psi_{x,1} & \Psi_{x,2} & \Psi_{x,3} & 0 & 0 & 0 \\ \Psi_{y,1} & \Psi_{y,2} & \Psi_{y,3} & \Psi_{y,4} & 0 & 0 \\ 0 & 0 & 0 & 0 & \Psi_{z,5} & \Psi_{z,6} \\ \Psi_{\dot{x},1} & \Psi_{\dot{x},2} & \Psi_{\dot{x},3} & 0 & 0 & 0 \\ \Psi_{\dot{y},1} & \Psi_{\dot{y},2} & \Psi_{\dot{y},3} & \Psi_{\dot{y},4} & 0 & 0 \\ 0 & 0 & 0 & 0 & \Psi_{\dot{z},5} & \Psi_{\dot{z},6} \end{bmatrix} \begin{bmatrix} K_1 \\ K_2 \\ K_3 \\ K_4 \\ K_5 \\ K_6 \end{bmatrix} \quad (49)$$

In this form, the non-dimensional coefficients are defined by the following:

$$\begin{aligned}
\Psi_{x,1} &= \frac{1}{k} + \frac{3}{2}k'\tau & \Psi_{x,2} &= \sin f & \Psi_{x,3} &= \cos f \\
\Psi_{y,1} &= -\frac{3}{2}k\tau & \Psi_{y,2} &= \left(1 + \frac{1}{k}\right) \cos f & \Psi_{y,3} &= -\left(1 + \frac{1}{k}\right) \sin f & \Psi_{y,4} &= \frac{1}{k} \\
\Psi_{z,5} &= \frac{1}{k} \sin f & \Psi_{z,6} &= \frac{1}{k} \cos f \\
\Psi_{\dot{x},1} &= \frac{k'}{2} - \frac{3}{2}k^2(k-1)\tau & \Psi_{\dot{x},2} &= k^2 \cos f & \Psi_{\dot{x},3} &= -k^2 \sin f \\
\Psi_{\dot{y},1} &= -\frac{3}{2}(k+k^2k'\tau) & \Psi_{\dot{y},2} &= -(k^2+1) \sin f & \Psi_{\dot{y},3} &= -e - (k^2+1) \cos f & \Psi_{\dot{y},4} &= -k' \\
\Psi_{\dot{z},5} &= e + \cos f & \Psi_{\dot{z},6} &= -\sin f
\end{aligned}$$

For readability, the auxiliary variables are given by:

$$\begin{aligned}
k &= 1 + e \cos f & k' &= \frac{dk}{df} = -e \sin f \\
\eta &= \sqrt{1 - e^2} & \tau &= \int_{f_0}^f \frac{df}{k^2} = \frac{nt}{\eta^3}
\end{aligned}$$

Given the defined initial relative position and velocity, the six integration constants  $K_1$  to  $K_6$  may be obtained using the preceding equations. It is observed that the constants  $K_1$  and  $K_2$  are orders of magnitude smaller than the others.

$$\begin{bmatrix} K_1 \\ K_2 \\ K_3 \\ K_4 \\ K_5 \\ K_6 \end{bmatrix} = \begin{bmatrix} 7.278 \times 10^{-10} \\ 5.571 \times 10^{-10} \\ -3.430 \times 10^{-5} \\ -2.678 \times 10^{-6} \\ 2.050 \times 10^{-5} \\ -2.050 \times 10^{-5} \end{bmatrix}$$

### 3.2.c Yamanaka-Ankersen Solution

To solve for the relative motion, we propagate time and calculate the mean anomaly from the time elapsed. From mean anomaly, the eccentric anomaly is obtained through the Newton-Raphson algorithm, and finally true anomaly is determined from the definition in Eqn. 7. The relative state can then be calculated at each time step from true anomaly by Equation 49. The propagated relative motion over 15 orbits is observed to be safe and periodic as shown in Figure 24 and Figure 25.

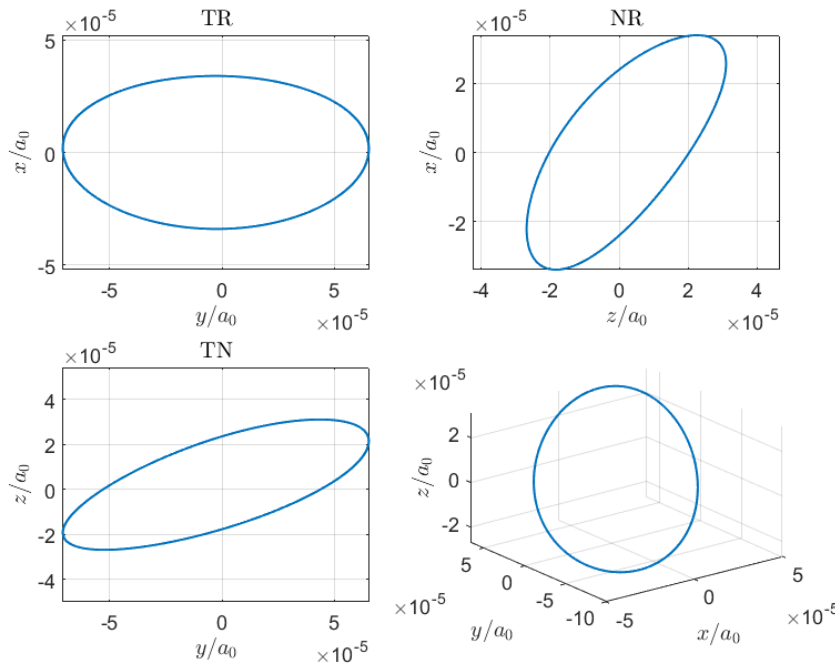


Figure 24: Analytically solved relative RTN position from YA solution over 15 orbits.

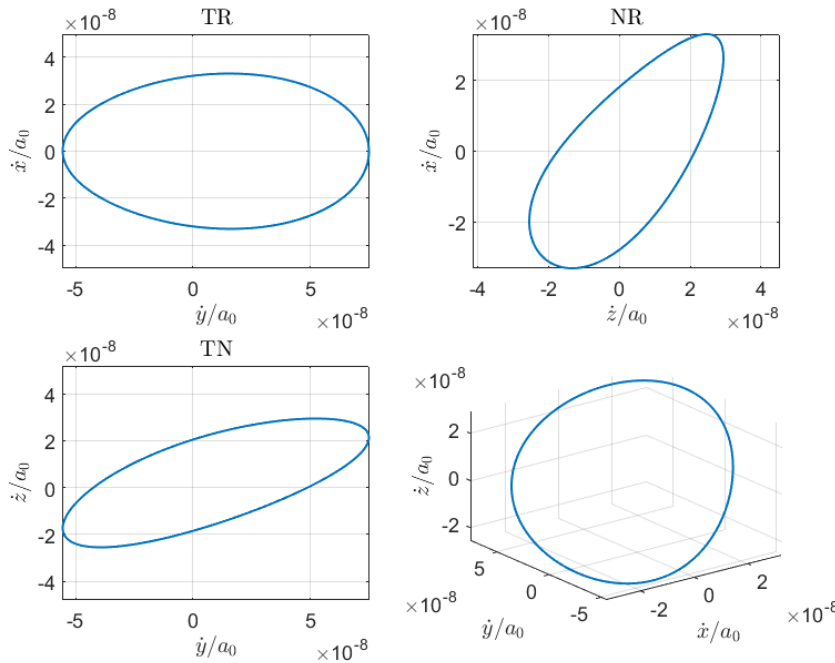


Figure 25: Analytically solved relative RTN velocity from YA solution over 15 orbits.

### 3.2.d Discussion of YA Solution

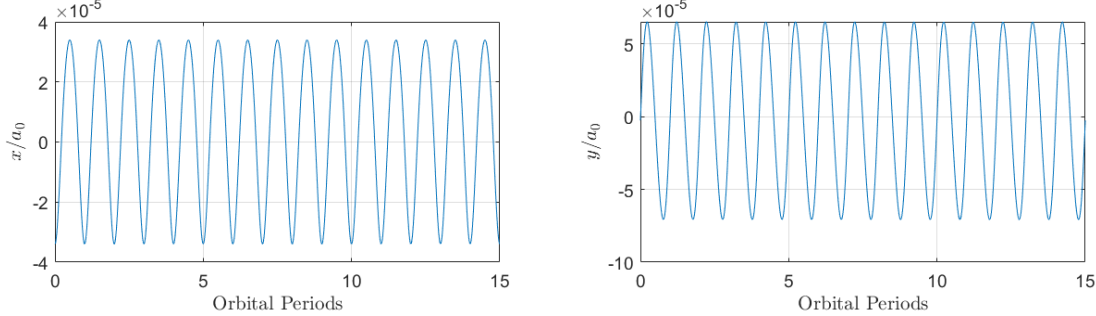


Figure 26: Analytically solved relative RTN position from YA solution.

Given the nature of the state transition matrix (STM) in Equation 49, we generally expect unbounded motion in  $x$  and  $y$ , and bounded periodic motion in  $z$ . As can be seen by the terms containing  $\tau$ , the  $\bar{x}$  and  $\bar{y}$  positions grow with time, resulting in an along-track drift and a growing amplitude in radial position over time. However, from Figure 24, we do not see any unbounded motion. Plots of  $x$  and  $y$  relative position over time in Figure 26 confirms the motion is periodic. The reason for this becomes clear when we consider the integration constants. Although unbounded motion may be expected by definition of the STM, the elements in the STM responsible for secular behavior are multiplied by  $K_1$ . From 3.2.b, the value of this integration constant is negligibly small (on the order of  $10^{-10}$ ), which leads to a unnoticeably unbounded motion over 15 orbits. We might expect this minute unbounded motion to appear after many orbits. To suppress instabilities in the YA solution, the motion may be bounded by choosing relative orbit parameters that allow  $K_1 = 0$ .

### 3.2.e Quasi-Nonsingular Relative Orbit Elements

The quasi-nonsingular relative orbit elements can be expressed as a linear combination of the absolute elements of the chief and deputy [9]. For the defined initial conditions, these evaluate to:

$$\begin{bmatrix} \delta a \\ \delta \lambda \\ \delta e_x \\ \delta e_y \\ \delta i_x \\ \delta i_y \end{bmatrix} = \begin{bmatrix} (a_1 - a_0)/a_0 \\ (u_1 - u_0) + (\Omega_1 - \Omega_0) \cos i_0 \\ e_{x1} - e_{x0} \\ e_{y1} - e_{y0} \\ i_1 - i_0 \\ (\Omega_1 - \Omega_0) \sin i_0 \end{bmatrix} = \begin{bmatrix} 0 \\ -2.677 \times 10^{-6} \\ 3.395 \times 10^{-5} \\ 0 \\ 2.050 \times 10^{-5} \\ 2.050 \times 10^{-5} \end{bmatrix}$$

These relations may be used to map orbital elements to relative position in the RTN frame as described in the next section.

### 3.2.f Relative Orbital Elements Geometric Linear Mapping

For eccentric orbits, a geometric mapping relates the RTN relative position at time  $t$  to the quasi-nonsingular relative orbital elements at initial time  $t_0 = 0$  [10]. The mapping mirrors the YA solution, where the integration constants are replaced by the quasi-nonsingular orbit elements as given by:

$$\begin{bmatrix} x \\ y \\ z \\ \dot{x} \\ \dot{y} \\ \dot{z} \end{bmatrix} = \begin{bmatrix} a\eta^2 I_{3 \times 3} & 0_{3 \times 3} \\ 0_{3 \times 3} & \frac{an}{\eta} I_{3 \times 3} \end{bmatrix} \begin{bmatrix} b_{x,1} & b_{x,2} & b_{x,3} & b_{x,4} & 0 & b_{x,6} \\ b_{y,1} & b_{y,2} & b_{y,3} & b_{y,4} & 0 & b_{y,6} \\ 0 & 0 & 0 & 0 & b_{z,5} & b_{z,6} \\ b_{\dot{x},1} & b_{\dot{x},2} & b_{\dot{x},3} & b_{\dot{x},4} & 0 & b_{\dot{x},6} \\ b_{\dot{y},1} & b_{\dot{y},2} & b_{\dot{y},3} & b_{\dot{y},4} & 0 & b_{\dot{y},6} \\ 0 & 0 & 0 & 0 & b_{\dot{z},5} & b_{\dot{z},6} \end{bmatrix} \begin{bmatrix} \delta a \\ \delta \lambda \\ \delta e_x \\ \delta e_y \\ \delta i_x \\ \delta i_y \end{bmatrix} \quad (50)$$

The non-dimensional coefficients are defined by:

$$\begin{aligned} b_{x,1} &= \frac{1}{k} + \frac{3}{2} k' \frac{n}{\eta^3} t & b_{x,3} &= \frac{1}{\eta^3} \left[ e_x \left( \frac{k-1}{1+\eta} \right) - \cos u \right] \\ b_{x,2} &= -\frac{k'}{\eta^3} & b_{x,4} &= \frac{1}{\eta^3} \left[ c_y \left( \frac{k-1}{1+\eta} \right) - \sin u \right] \\ b_{x,6} &= \frac{k'}{\eta^3} \cot i & & \\ b_{y,1} &= -\frac{3}{2} k \frac{n}{\eta^3} t & b_{y,3} &= \frac{1}{\eta^2} \left[ \left( 1 + \frac{1}{k} \right) \sin u + \frac{e_y}{k} + \frac{k}{\eta} \left( \frac{e_y}{1+\eta} \right) \right] \\ b_{y,2} &= \frac{k}{\eta^3} & b_{y,4} &= -\frac{1}{\eta^2} \left[ \left( 1 + \frac{1}{k} \right) \cos u + \frac{e_x}{k} + \frac{k}{\eta} \left( \frac{e_x}{1+\eta} \right) \right] \\ b_{y,6} &= \left( \frac{1}{k} - \frac{k}{\eta^3} \right) \cot i & & \\ b_{z,5} &= \frac{1}{k} \sin u & b_{z,6} &= -\frac{1}{k} \cos u \\ b_{\dot{x},1} &= \frac{k'}{2} + \frac{3}{2} k^2 (1-k) \frac{n}{\eta^3} t & b_{\dot{x},3} &= \frac{k^2}{\eta^3} \left[ \eta \sin u + e_y \left( \frac{k-1}{1+\eta} \right) \right] \\ b_{\dot{x},2} &= \frac{k^2}{\eta^3} (k-1) & b_{\dot{x},4} &= -\frac{k^2}{\eta^3} \left[ \eta \cos u + e_x \left( \frac{k-1}{1+\eta} \right) \right] \\ b_{\dot{x},6} &= -\frac{k^2}{\eta^3} (k-1) \cot i & & \\ b_{\dot{y},1} &= -\frac{3}{2} k \left( 1 + kk' \frac{n}{\eta^3} t \right) & b_{\dot{y},3} &= \left( 1 + \frac{k^2}{\eta^3} \right) \cos u + e_x \frac{k}{\eta^2} \left[ 1 + \frac{k}{\eta} \left( \frac{1-k}{1+\eta} \right) \right] \\ b_{\dot{y},2} &= \frac{k^2}{\eta^3} k' & b_{\dot{y},4} &= \left( 1 + \frac{k^2}{\eta^3} \right) \sin u + e_y \frac{k}{\eta^2} \left[ 1 + \frac{k}{\eta} \left( \frac{1-k}{1+\eta} \right) \right] \\ b_{\dot{y},6} &= -\left( 1 + \frac{k^2}{\eta^3} \right) k' \cot i & & \end{aligned}$$

By propagating the true anomaly as the independent variable, relative motion in the RTN frame may be obtained. The resulting position and velocity, normalized by the semi-major axis of the chief is plotted on top of the YA solution in Figure 27 and Figure 28. The solutions overlap closely as there are small errors between them.

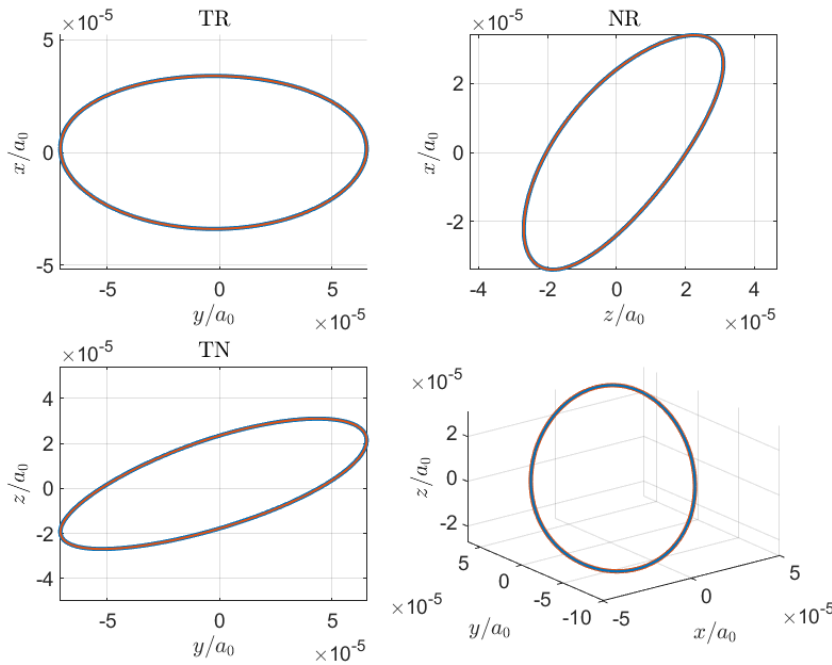


Figure 27: Analytically solved relative RTN position from YA solution (blue) and geometric linear mapping (red).

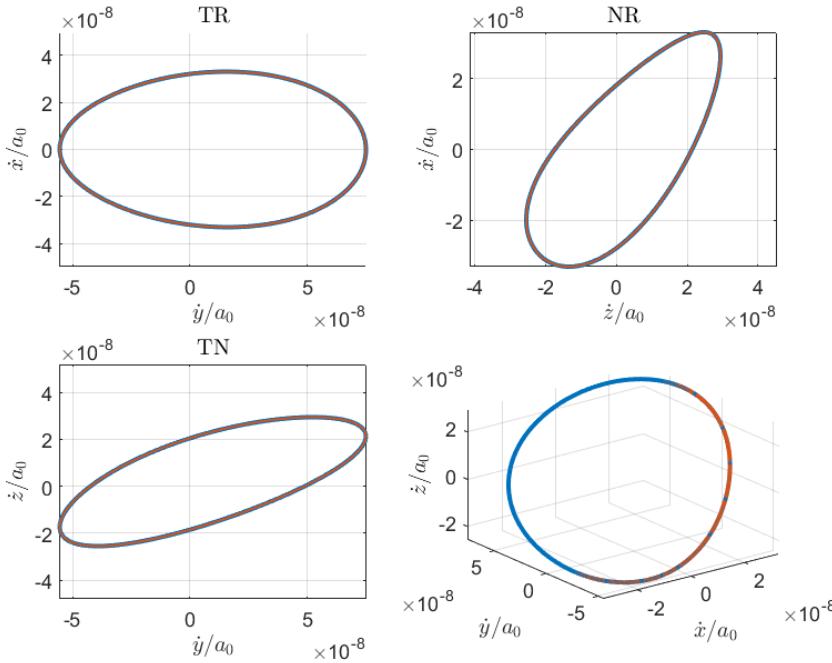


Figure 28: Analytically solved relative RTN velocity from YA solution (blue) and geometric linear mapping (red).

### 3.2.g Comparison between Relative Orbital Elements and YA Integration Constants

Although the geometric mapping updates position and velocity differently, the end result is nearly indistinguishable. The results shown in Figure 27 are to be expected given the integration constants and the relative orbital parameters:

$$\begin{bmatrix} \delta a \\ \delta \lambda \\ \delta e_x \\ \delta e_y \\ \delta i_x \\ \delta i_y \end{bmatrix} = \begin{bmatrix} 0 \\ -2.677 \times 10^{-6} \\ 3.395 \times 10^{-5} \\ 0 \\ 2.050 \times 10^{-5} \\ 2.050 \times 10^{-5} \end{bmatrix}$$

$$\begin{bmatrix} K_1 \\ K_2 \\ K_3 \\ K_4 \\ K_5 \\ K_6 \end{bmatrix} = \begin{bmatrix} 7.278 \times 10^{-10} \\ 5.571 \times 10^{-10} \\ -3.430 \times 10^{-5} \\ -2.678 \times 10^{-6} \\ 2.050 \times 10^{-5} \\ -2.050 \times 10^{-5} \end{bmatrix}$$

At first glance these are not the same, but we do notice that if we compare the values individually, there are a lot of similarities. The first two integration constants  $K_1$  and  $K_2$  are close to 0, matching  $\delta a$  and  $\delta e_y$ .  $K_3$  matches well with the  $\delta e_x$ , and  $K_4$  with the  $\delta \lambda$ . The last two integration constants  $K_5$  and  $K_6$  match the same magnitude as the relative inclination vector. There are some differences in the values and the phases (numeric sign), but in general the orders of magnitude are quite similar. This equivalence can be confirmed by mapping from the integration constants to the ROEs by the defined relation:

$$\begin{bmatrix} \delta a \\ \delta \lambda_0 \\ \delta e_x \\ \delta e_y \\ \delta i_x \\ \delta i_y \end{bmatrix} = \begin{bmatrix} 1 & 0 & 0 & 0 & 0 & 0 \\ 0 & -e_x \left( \eta + \frac{1}{1+\eta} \right) & e_y \left( \eta + \frac{1}{1+\eta} \right) & 1 & 0 & 0 \\ 0 & e_x e_y & e_x^2 - 1 & -e_y & 0 & -e_y \cot i \\ 0 & e_y^2 - 1 & e_x e_y & e_x & 0 & e_x \cot i \\ 0 & 0 & 0 & 0 & 1 & 0 \\ 0 & 0 & 0 & 0 & 0 & -1 \end{bmatrix} \begin{bmatrix} K_1 \\ K_2 \\ K_3 \\ K_4 \\ K_5 \\ K_6 \end{bmatrix}_u = \begin{bmatrix} 7.278 \times 10^{-10} \\ -2.678 \times 10^{-6} \\ 3.395 \times 10^{-5} \\ -6.741 \times 10^{-10} \\ 2.050 \times 10^{-5} \\ 2.050 \times 10^{-5} \end{bmatrix}$$

In constructing this mapping, we clearly see that the integration constants resemble the relative orbital elements except for small numerical variations.

### 3.2.h True Relative Propagation

To calculate the true relative position, we numerically integrate the non-linear relative equations of motion as described in 2.1.b. The result is plotted alongside the YA solution and the geometric mapping in Figure 29 and Figure 30, again demonstrating the numerical accuracy of the solutions with each other.

Figure 31 shows the errors compared to the true relative propagation from numerical integration. Error in the radial and along-track components using the TH equations in 3.2.c increases with the number of orbits, while the error using the geometric mapping appears to remain periodic and smaller by comparison. Higher accuracy observed in the geometric mapping model may be attributed to the use of relative orbital elements. Since ROEs describe angles rather than approximate Cartesian position as in the TH solution, higher-order errors in geometric mapping are smaller.

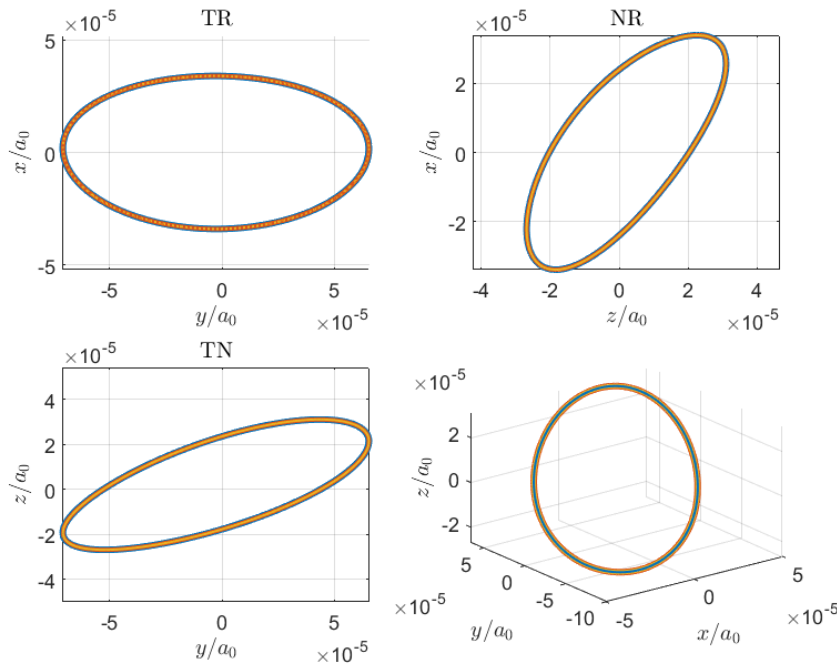


Figure 29: Analytically solved relative RTN position from YA solution (blue), geometric linear mapping (red), and numerical integration (yellow).

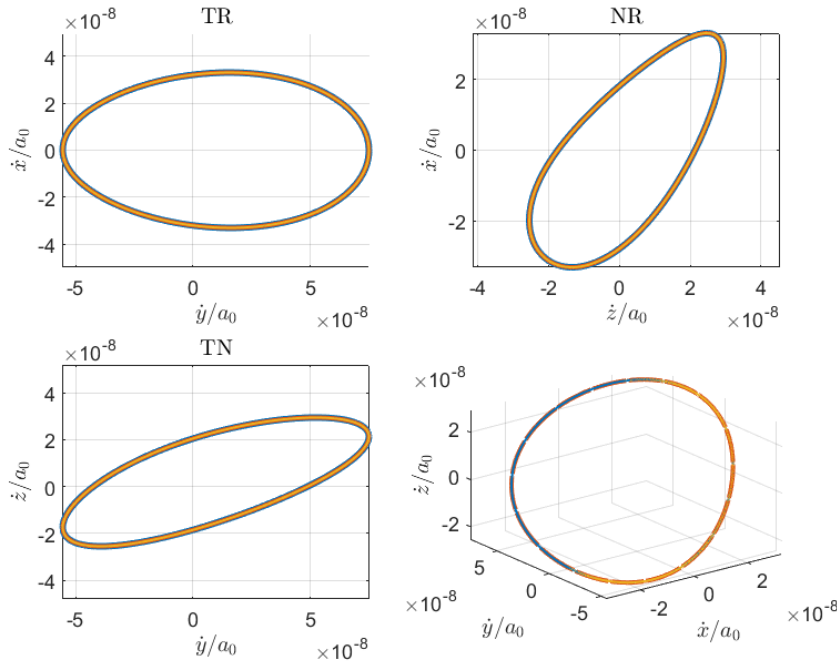


Figure 30: Analytically solved relative RTN velocity from YA solution (blue), geometric linear mapping (red), and numerical integration (yellow).

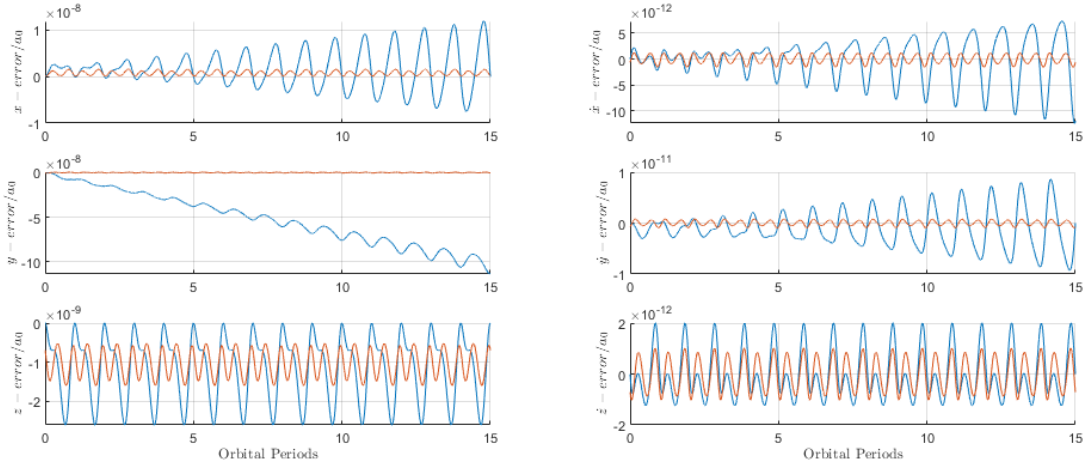


Figure 31: Error in the analytically solved relative RTN velocity from YA solution (blue), and geometric linear mapping (red).

### 3.2.i Difference in Semi-major Axis & Highly Eccentric Orbits

We repeat this analysis first by removing the energy matching condition. This means that we no longer have the same semi-major axis for the chief and deputy. As done in 2.1.d, we offset the deputy semimajor axis by  $\delta a = 100 \text{ m}$ . Given this separation, we expect that the deputy will move slower than the chief, and so we should see a drift in the TR plane. Increasing the semi-major axis of the deputy leads to it falling behind, so the ellipse should trail to the left. The quasi-singular relative orbital parameters are:

$$\begin{bmatrix} \delta a \\ \delta \lambda \\ \delta e_x \\ \delta e_y \\ \delta i_x \\ \delta i_y \end{bmatrix} = \begin{bmatrix} 1.306 \times 10^{-5} \\ -2.677 \times 10^{-6} \\ 3.395 \times 10^{-5} \\ 0 \\ 2.050 \times 10^{-5} \\ 2.050 \times 10^{-5} \end{bmatrix}$$

The leftward motion (growing relative distance) is confirmed in Figure 32.

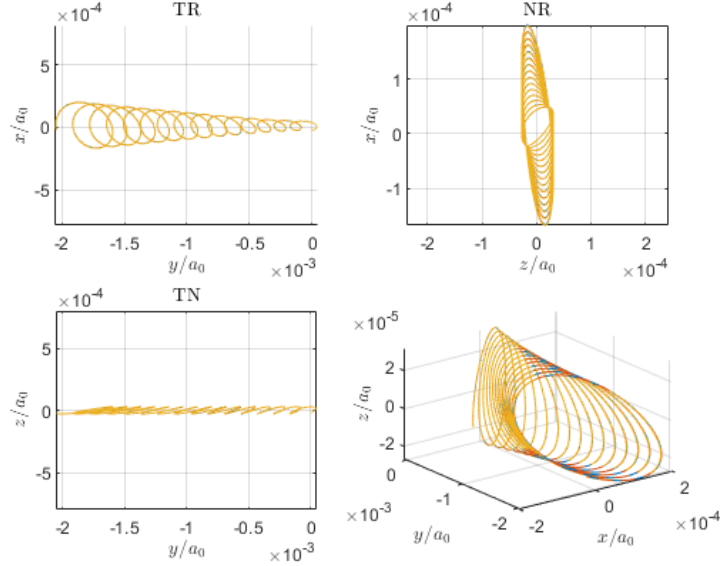


Figure 32: Analytically solved relative RTN position from YA solution (blue), geometric linear mapping (red), and numerical integration (yellow) for non-energy matched chief and deputy.

Next, we investigate the effects of large differences in semi-major axis. In Figure 33, we impose  $\delta a = -10,000 \text{ m}$ . This allows us to both observe the effects of negative semi-major axis changes as well as the limit of our linear approximations (YA and geometric mapping). We observe that over the course of 15 orbits, our linear approximations diverge greatly from the nonlinear numerical integration, indicating that these approximations may no longer be appropriate for large initial relative separations.

$$\begin{bmatrix} \delta a \\ \delta \lambda \\ \delta e_x \\ \delta e_y \\ \delta i_x \\ \delta i_y \end{bmatrix} = \begin{bmatrix} -0.0013 \\ -2.677 \times 10^{-6} \\ 3.395 \times 10^{-5} \\ 0 \\ 2.050 \times 10^{-5} \\ 2.050 \times 10^{-5} \end{bmatrix}$$

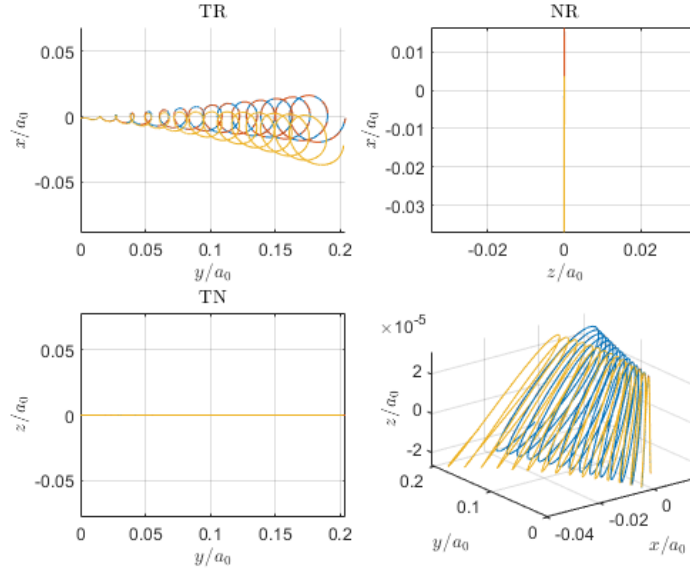


Figure 33: Analytically solved relative RTN position from YA solution (blue), geometric linear mapping (red), and numerical integration (yellow) for large initial relative separation.

Next, we look to investigate highly elliptic orbits. Here we select the chief orbit eccentricity to be  $e_0 = 0.6$ . The quasi-singular relative orbital parameters are found to be:

$$\begin{bmatrix} \delta a \\ \delta \lambda \\ \delta e_x \\ \delta e_y \\ \delta i_x \\ \delta i_y \end{bmatrix} = \begin{bmatrix} 0 \\ -1.190 \times 10^{-6} \\ 1.509 \times 10^{-5} \\ 0 \\ 9.110 \times 10^{-6} \\ 9.110 \times 10^{-6} \end{bmatrix}$$

Though in theory we are only changing the eccentricity, the relative inclination vector also seems to change. This occurs because of the way the semi-major axis is calculated. The periapsis was taken to be equivalent to the semi-major axis of 3.1 (the near-circular orbit case), and then the new semi-major axis was found from this and the desired eccentricity. Therefore, the relative inclination vector changes because it is normalized by the semi-major axis.

The results comparing the three relative motion methods are shown in Figure 34. As expected, the relative position is now deformed from the previous elliptical shape in the TR plane, but safe relative orbit is still maintained. Some numerical instability was observed in calculations of the eccentric anomaly. This was mitigated by adding a check ensuring that the eccentric anomaly is propagated in small steps to prevent significant non-physical jumps in angle value.

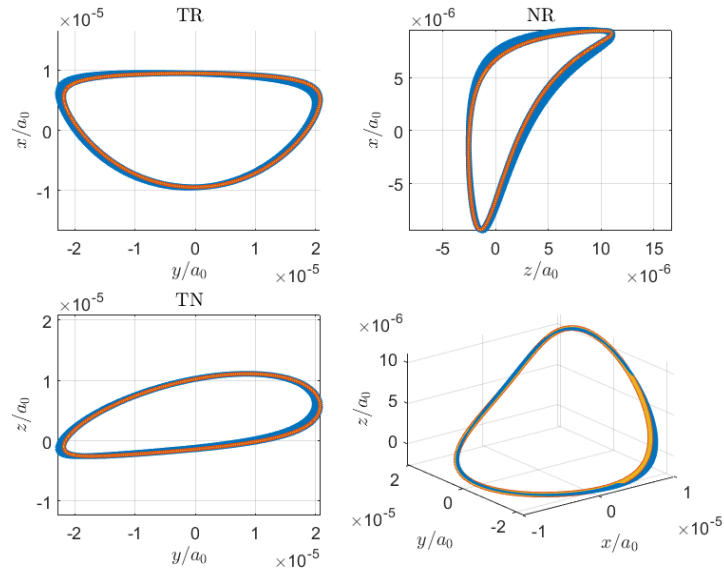


Figure 34: Analytically solved relative RTN position from YA solution (blue), geometric linear mapping (red), and numerical integration (yellow) for non-energy matched chief and deputy.

## 4 References

- [1] H. J. Kramer. “Tdx (tandem-x).” (Sep. 2016), [Online]. Available: <https://www.eoportal.org/satellite-missions/tandem-x>.
- [2] G. Krieger, A. Moreira, H. Fiedler, *et al.*, “TanDEM-x: A satellite formation for high-resolution SAR interferometry,” *IEEE Transactions on Geoscience and Remote Sensing*, vol. 45, no. 11, pp. 3317–3341, Nov. 2007, ISSN: 1558-0644. DOI: [10.1109/TGRS.2007.900693](https://doi.org/10.1109/TGRS.2007.900693).
- [3] H. J. Kramer. “Tsx (terrasar-x).” (Jun. 2012), [Online]. Available: <https://www.eoportal.org/satellite-missions/terrasar-x>.
- [4] A. I. Flores-Anderson, K. E. Herndon, R. B. Thapa, and E. Cherrington, *The Synthetic Aperture Radar (SAR) Handbook: Comprehensive Methodologies for Forest Monitoring and Biomass Estimation*. SERVIR Global Science Coordination Office, Apr. 2019. DOI: [10.25966/nr2c-s697](https://doi.org/10.25966/nr2c-s697).
- [5] R. R. Bate, D. D. Mueller, and J. E. White, *Fundamentals of astrodynamics*, en. New York: Dover Publications, 1971, ISBN: 978-0-486-60061-1.
- [6] D. A. Vallado, *Fundamentals of Astrodynamics and Applications*. 1997.
- [7] K. T. Alfriend, S. R. Vadali, P. Gurfil, J. P. How, and L. S. Breger, *Spacecraft Formation Flying: Dynamics, Control, and Navigation*. Elsevier Astrodynamics Series, 2010.
- [8] O. Montenbruck, R. Kahle, S. D’Amico, and J.-S. Ardaens, “Navigation and control of the TanDEM-x formation,” *The Journal of the Astronautical Sciences*, vol. 56, no. 3, pp. 341–357, Sep. 1, 2008, ISSN: 0021-9142. DOI: [10.1007/BF03256557](https://doi.org/10.1007/BF03256557). [Online]. Available: <https://doi.org/10.1007/BF03256557>.
- [9] S. D’Amico, “Autonomous formation flying in low earth orbit,” Ph.D. dissertation, Technical University of Delft, 2010.
- [10] M. B. Willis, “Analytical theory of satellite relative motion with applications to autonomous navigation and control,” Ph.D. dissertation, Stanford University, 2023.

## 5 Appendix A: Code

All code for this project can be found in the following [GitHub repository](#).